REPORT DOCUMENTATION PAGE

Form Approved OMB NO. 0704-0188

1. REPORT DATE (DD-MM-YYYY) 18-06-2012	2. REPORT TYPE Final Report	3. DATES COVERED (From - To) 1-Oct-2006 - 31-Mar-2012

4. TITLE AND SUBTITLE Microstructurally Engineered Armor System for Enhanced Survivability through Optimum Energy and Momentum Dissipation	5a. CONTRACT NUMBER W911NF-06-1-0472
	5b. GRANT NUMBER
	5c. PROGRAM ELEMENT NUMBER 121000
6. AUTHORS M.A. Zikry	5d. PROJECT NUMBER
	5e. TASK NUMBER
	5f. WORK UNIT NUMBER

7. PERFORMING ORGANIZATION NAMES AND ADDRESSES North Carolina State University Research Administration NC State University Raleigh, NC 27695 -7514	8. PERFORMING ORGANIZATION REPORT NUMBER

9. SPONSORING/MONITORING AGENCY NAME(S) AND ADDRESS(ES) U.S. Army Research Office P.O. Box 12211 Research Triangle Park, NC 27709-2211	10. SPONSOR/MONITOR'S ACRONYM(S) ARO
	11. SPONSOR/MONITOR'S REPORT NUMBER(S) 51981-EG-JDO.11

12. DISTRIBUTION AVAILIBILITY STATEMENT

Approved for Public Release; Distribution Unlimited

13. SUPPLEMENTARY NOTES

14. ABSTRACT

This project is focused on the optimization and development of a new class of high strength and lightweight aluminum alloys for armored systems subjected to high rate and severe loading conditions associated with IED events. The current effort is led by North Carolina State University (M.A. Zikry, D. Brenner, NCSU) An integrated experimental and atomistic and microstructural modeling framework has been developed and used to rapidly identify dominant microstructural characteristics that have been used to significantly improve ballistic response

15. SUBJECT TERMS

Microstructure, multiscale computational modeling, aluminum

16. SECURITY CLASSIFICATION OF:			17. LIMITATION OF ABSTRACT	15. NUMBER OF PAGES	19a. NAME OF RESPONSIBLE PERSON Mohammed Zikry
a. REPORT UU	b. ABSTRACT UU	c. THIS PAGE UU	UU		19b. TELEPHONE NUMBER 919-515-5237

Microstructurally Engineered Armor System for Enhanced Survivability through Optimum Energy and Momentum Dissipation

ABSTRACT

This project is focused on the optimization and development of a new class of high strength and lightweight aluminum alloys for armored systems subjected to high rate and severe loading conditions associated with IED events. The current effort is led by North Carolina State University (M.A. Zikry, D. Brenner, NCSU) An integrated experimental and atomistic and microstructural modeling framework has been developed and used to rapidly identify dominant microstructural characteristics that have been used to significantly improve ballistic response through tailored processing for desired applications. The project has resulted in new state-of-the-art in the aluminum armor alloy technology, and aims to develop very high mass efficiency aluminum armor alloys that are resistant to blast and penetrative events. This research is providing a critical link between macroscopic dynamic response, microstructural characteristics and inelastic mechanisms at relevant length and time scales. This basic research is being transitoned to the ARL – WMRD where it is being used to enrich parallel research efforts and help develop new and significantly improved armor designs.

Enter List of papers submitted or published that acknowledge ARO support from the start of the project to the date of this printing. List the papers, including journal references, in the following categories:

(a) Papers published in peer-reviewed journals (N/A for none)

Received	Paper
2012/06/11 2 10	. Incompatibility Based Fracture, Philosophical Magazine, (10 2012): 0. doi:
2012/06/02 1! 14	K.I. Elkhodary, M.A. Zikry. A fracture criterion for finitely deforming crystalline solids—The dynamic fracture of single crystals, Journal of the Mechanics and Physics of Solids, (10 2011): 2007. doi: 10.1016/j.jmps.2011.07.004
2012/06/02 1! 13	K. Elkhodary, W. Lee, L.P. Sun, D.W. Brenner, M.A. Zikry. Deformation mechanisms of an ? precipitate in a high-strength aluminum alloy subjected to high strain rates, Journal of Materials Research, (02 2011): 487. doi: 10.1557/jmr.2010.29
2012/06/02 1ₐ 12	W. M. Lee, M. A. Zikry. Microstructural Characterization of a High-Strength Aluminum Alloy Subjected to High Strain-Rate Impact, Metallurgical and Materials Transactions, (12 2010): 0. doi: 10.1007/s11661-010-0476-z
2012/05/25 1(6	W.M. Lee, M.A. Zikry. Modeling the interfacial plastic strain incompatibilities associated with dispersed particles in high strength aluminum alloys, Acta Materialia, (2 2012): 0. doi: 10.1016/j.actamat.2011.11.058
2012/05/25 1(5	W.M. Lee, M.A. Zikry. Dispersed particle and triple junction interactions in aluminum alloys, Materials Science and Engineering: A, (2 2012): 0. doi: 10.1016/j.msea.2011.12.081
2012/05/25 1(4	H. G. Salem, William M. Lee, Laurence Bodelot, G. Ravichandran, M. A. Zikry. Quasi-Static and High-Strain-Rate Experimental Microstructural Investigation of a High-Strength Aluminum Alloy, Acta Materialia, (1 2012): 0. doi: 10.1007/s11661-011-1064-6

TOTAL: **7**

Number of Papers published in peer-reviewed journals:

(b) Papers published in non-peer-reviewed journals (N/A for none)

   TOTAL: **1**

Number of Papers published in non peer-reviewed journals:

(c) Presentations

1. Experimental and Microstructurally-Based Computational Investigation of the High Strain-Rate Behavior of High Strength Aluminum Alloys, The Metals Society, Orlando, FL, March, 2012
2. Failure Modes in High Strength Aluminum Alloys, ASME IMECE 201, Denver, 2011.
3. Experimental and Microstructurally-Based Computational Investigation of the High Strain-Rate Behavior of High Strength Aluminum Alloys, The Metals Society, San Diego, CA, March, 2011
4. Dislocation-Density Evolution in Crystalline Solids, ASME IMECE 2010, Vancouver, 2010.
5. Deformation Modes in Aluminum, ASME IMECE 2010, Vancouver, 2010.
Failure Modes in Aluminum Alloys (2010), 16th US National Congress on Theoretical and Applied Mechanics, The Pennsylvania State University, University Park, PA
6. High Strength Aluminum Alloy Behavior, The Metals Society, Seattle, WA, February, 2010.
7. Modeling of High Strength Aluminum Alloys, Materials Research Society Meeting, Boston, MA, 2009.
8. Microstructural Modeling of Failure Modes in Crystalline Materials, ASME IMECE 2009, Orlando, FL, 2009.
9. High strength Aluminum Alloy Behavior, ASME IMECE 2009, Orlando, FL, 2009.
10. Microstructural Modeling of Failure Modes in Crystalline Materials, X International Conference on Computational Plasticity, Barcelona, Spain, 2009.
11. Microstructural Modeling of Failure Modes in Crystalline Materials, 12th International Conference on Fracture, Ottawa, Canada, 2009.
12. Modeling and Experiments of High Strength Aluminum Alloys, ASME Summer Mechanics Meeting, Blacksburg, VA, 2009
13. •Experimental and Computational Investigation of High Strength Aluminum Alloys, The Metals Society Annual Meeting, San Francisco, CA, February, 2009

Number of Presentations: 13.00

Non Peer-Reviewed Conference Proceeding publications (other than abstracts):

Number of Non Peer-Reviewed Conference Proceeding publications (other than abstracts):

Peer-Reviewed Conference Proceeding publications (other than abstracts):

Number of Peer-Reviewed Conference Proceeding publications (other than abstracts):

(d) Manuscripts

Received		Paper
2011/09/13 2:	2	K.ELKHODARY, M.A. Zikry. Deformation mechanisms of an ? precipitate in a high strength aluminum alloy subjected to high strain rates , Journal of Materials Research (09 2010)
2011/09/13 2:	1	K.ElKhodary, M.A. Zikry. A Fracture Criterion for Finitely Deforming Crystalline Solids -The Dynamic Fracture of Single Crystals, Journal of Mechanics Physics Solids (07 2011)
2011/09/13 2:	3	. Microstructural Characterization of a High Strength Aluminum Alloy Subjected to High Strain-Rate Impact, (05 2011)

TOTAL: **3**

Number of Manuscripts:

Books

Received	Paper

TOTAL:

Patents Submitted

Patents Awarded

Awards

Cover of the Journal of Materials Research, Cambridge Press, March 2011
• Distinguished Research Award, NCSU, 2010
• Outstanding Paper with K. El-Khodary, W.M. Lee, L. Sun, and D. Brenner, Symposium HH Materials Research Society, 2009, Feature Article, Journal of Materials Research, 2010
• Jefferson Science Fellow, U.S. State Department, 2008-Present

---

Graduate Students

NAME	PERCENT_SUPPORTED	Discipline
K. El-Khodary	1.00	
William Lee	1.00	
FTE Equivalent:	**2.00**	
Total Number:	**2**	

Names of Post Doctorates

NAME	PERCENT_SUPPORTED
O. Rezvanian	1.00
L. Sun	1.00
FTE Equivalent:	**2.00**
Total Number:	**2**

Names of Faculty Supported

NAME	PERCENT SUPPORTED	National Academy Member
D. Brenner	0.20	
G. Ravichandran	0.10	
M.A. Zikry	0.20	
FTE Equivalent:	**0.50**	
Total Number:	**3**	

Names of Under Graduate students supported

NAME	PERCENT_SUPPORTED
FTE Equivalent:	
Total Number:	

Student Metrics
This section only applies to graduating undergraduates supported by this agreement in this reporting period

The number of undergraduates funded by this agreement who graduated during this period: 0.00

The number of undergraduates funded by this agreement who graduated during this period with a degree in science, mathematics, engineering, or technology fields:...... 0.00

The number of undergraduates funded by your agreement who graduated during this period and will continue to pursue a graduate or Ph.D. degree in science, mathematics, engineering, or technology fields:...... 0.00

Number of graduating undergraduates who achieved a 3.5 GPA to 4.0 (4.0 max scale):...... 0.00

Number of graduating undergraduates funded by a DoD funded Center of Excellence grant for Education, Research and Engineering:...... 0.00

The number of undergraduates funded by your agreement who graduated during this period and intend to work for the Department of Defense 0.00

The number of undergraduates funded by your agreement who graduated during this period and will receive scholarships or fellowships for further studies in science, mathematics, engineering or technology fields:...... 0.00

Names of Personnel receiving masters degrees

NAME
Total Number:

Names of personnel receiving PHDs

NAME
K. ElKhodary
W Lee
Total Number: 2

Names of other research staff

NAME	PERCENT_SUPPORTED
FTE Equivalent:	
Total Number:	

Sub Contractors (DD882)

Scientific Progress

This project was focused on the optimization and development of a new class of high strength and lightweight aluminum alloys for armored systems subjected to high rate and severe loading conditions associated with IED events. The current effort is led by North Carolina State University (M.A. Zikry, D. Brenner, NCSU) in cooperation with the California Institute of Technology (G. Ravichandran), and the Army Research Laboratory – Weapons and Materials Research Directorate (B. Cheeseman, ARL/WMRD). An integrated experimental and atomistic and microstructural modeling framework has been used to rapidly identify dominant microstructural characteristics that have been used to significantly improve ballistic response through tailored processing for desired applications. The project has resulted in new state-of-the-art in the aluminum armor alloy technology, and aims to develop very high mass efficiency aluminum armor alloys that are resistant to blast and penetrative events. This research is providing a critical link between macroscopic dynamic response, microstructural characteristics and inelastic mechanisms at relevant length and time scales. This basic research is being transitoned to the ARL – WMRD where it is being used to enrich parallel applied research efforts and help develop new and significantly improved armor designs.

The ultimate objective was to develop a new class of high strength, blast resistant lightweight aluminum alloys. It should be noted that the ballistic evaluation of the 2139-T8 aluminum alloy has shown such significant promise that it has been evaluated under a number of armor programs at ARL. It has been qualified as a Long-Term Armor Strategy (LTAS), two Military Specifications are presently being developed for it, and it has been incorporated into the Stryker Underbody Kit. The project has developed unique and specialized multiscale modeling techniques, dynamic experiments, and characterization tools to develop mitigation strategies to defeat damage modes pertaining to IED blasts. There have been significant transitions with ALCAN, BAE, Touchstone, and ATI, where the computational techniques and optimization methods have been used to improve processing and synthesis techniques.

Some of the major accomplishments were:
- Identifying the major dominant mechanisms affecting behavior at different scales ranging from the atomistic to the macro
- Design guidelines for a new genration of aluminum that is blast resistant and damage tolerant
- New fracture Criteria tha is mesh independent that can be applied to DoD systems and applications
- Guidelines have been using in a mil-spec by ARL for aluminum systems.
In summary, a Microstructurally Engineered Armor Systems for Enhanced Survivability
through Optimum Energy and Momentum Dissipation Control has been developed.

Technology Transfer

ARO Final Report: High Strain-Rate Fracture and Failure In Aluminum Alloys

1. Introduction

The thermo-mechanical behavior of metals and alloys under dynamic loading conditions has to be accurately understood and predicted for the optimal design of myriad civilian and defense systems. For example, metal forming processes and ballistic applications require a detailed understanding of the dynamic behavior of alloys under large deformations and extreme loading conditions at different temporal and spatial scales. To obtain such an understanding, experiments are needed to characterize the mechanical properties of interest for each alloy, such as tensile strength, ductility, toughness, and strain-rate sensitivity. However, many other properties are difficult, if not impossible, to quantify experimentally, such as subsurface damage and local dynamic deformation and failure modes.

Aluminum, alloys such as 2024-Al and 2048-Al have been specifically tailored for use in applications that require high fracture toughness and crack propagation resistance, such as aircraft structures, automotive applications, armored vehicles, and electronic packaging devices. These alloys do not, however, perform well at high temperatures. Therefore, heat resistant alloys, such as 2219-Al and 2618-Al have been developed for applications that require high specific strength and high temperature capability. These heat resistant Al-Cu-Mg alloys, however, have limited fracture strength and damage tolerance [1]. Nonetheless, the addition of small amounts of Ag to Al-Cu-Mg alloys, with high Cu to Mg ratios can significantly improve the age hardening response by the nucleation of thermally stable, plate–like Ω precipitates on {111} planes in the aluminum matrix [2]. Moreover, Al-Cu-Mg-Ag alloys have less grain boundary (GB) precipitation, and therefore retain most of their toughness after age hardening, and are less susceptible to intergranular fracture [3, 4].

1

Therefore, Al-Cu-Mg-Ag alloys currently being developed can concurrently exhibit relatively high strength, thermal resistance, toughness, and damage tolerance. For example, the alloy 2139-T8, with Mn additions [5], has precipitates, dispersoids and constituents spanning multiple length scales, and has significantly improved fatigue life and fracture toughness in comparison to currently used alloys in the aerospace industry. The ballistic performance of 2139-Al has also been shown to be superior to that of Al-2519, which is used in armored vehicles [5].

The potential design of such Al-Cu-Mg-Ag alloys for different applications is therefore predicated on understanding, identifying, and optimizing the material mechanisms, which span length scales from the nano to the micro, related to increased strength and toughness. Specifically, if these alloys are to be tailored for ballistic applications, optimal trade-offs between competing requirements on strength and toughness have to be identified and controlled.

The major objective of this work has been to model within a continuum framework the dynamic failure of aluminum alloys with complex microstructures using a newly proposed *compatibility-based* fracture law. To model the nucleation and propagation of failure surfaces at the microstructural scale, we use finite deformation theory, to develop a specialized decomposition of the deformation gradient ($\mathbf{F}$), as an alternative to the Kroner-Lee decomposition, which is specific to crystalline solids. We then propose a general fracture criterion for finitely deforming crystals, based on the integral law of compatibility. Finite element analyses were conducted to elucidate the interactions of Mn-bearing dispersoids, Ω precipitates and θ' precipitates with dynamic fracture processes. Rate dependent crystalline plasticity was coupled with recently developed rational orientation relationships [6] to provide insights on crystalline and microstructural interaction mechanisms that govern large strain deformation and failure phenomena, such as dynamic localization, crack nucleation, propagation, and adiabatic heating, all of which are critical in determining the dynamic toughness and damage tolerance of alloys.

The outline of this paper is as follows: in Section 2, we outline our recently proposed compatibility-based theory for the dynamic fracture of crystalline solids. In Section 3, we outline

the constitutive formulations of crystalline plasticity and rational orientation of precipitates. The simulations for microstructural aggregates with Mn-bearing particles, Ω and θ' precipitates, and low angle boundaries are then presented and discussed in Sections 4 and 5. Finally, we summarize the salient findings in Section 6.

2. Fracture of Finitely-deforming Crystalline Solids

In this section we outline in some detail our recently developed δ-criterion for fracture, whose fuller development may be found in [7]. As an overview, cracks are assumed as topological defects. Hence, when a crack nucleates, the deformation (F), which maps a (compact) neighborhood of the reference continuum to the deformed configuration, must cease to satisfy compatibility. Now, in finite elements, it is always assumed that $F = \nabla_X u$, i.e. that the deformation map (F) is a gradient of a unique displacement field (u), tacitly implying its a priori satisfaction of compatibility, irrespective of the evolving kinetics. By setting up an independent calculation of F, splitting it according to the underlying physical mechanisms, we can monitor this assumption of compatibility throughout a simulation. This approach will define a compatibility-based fracture criterion δ; a vector whose magnitude (δ_s) serves as an indication of how reasonably a material point can satisfy compatible deformations via the modeled physical mechanisms. Mathematically, a non-zero δ requires the birth of a local topological defect, interpreted as a nucleating crack.

The δ-criterion applies to all crystalline solids insofar as they are modeled as Cauchy-type continua (i.e. classical continuum theory on which standard finite element codes are built), which follows from the very universality of the associated topological definitions (cf. [8-10]) of compactness and compatibility. This is true whether crystals exhibit ductile, brittle or mixed modes of failure, since they all must satisfy compatibility under the combined action of their crystal-specific mechanisms, which in Cauchy-type continua are fully accounted for in their locally evolving deformation maps (hence, F). The applicability of this same δ-criterion across dissimilar crystals (i.e. being a '*form-invariant*' criterion), are precisely what permit the

predictive modeling of the competing failure modes in microstructural aggregates. Hence, there is no need for: (1) a priori definition of fracture energies or crystal-specific fracture modes (see for example [11] for a review), or (2) combining crystal plasticity with cohesive zone models (cf. [12, 13]). These approaches would require, as input, fracture-specific information that is usually unavailable in materials whose properties are yet to be predicted, which is a difficulty that the compatibility-based δ-criterion has been developed to specifically address.

2.1 Decomposing the Deformation Gradient, F, in Crystalline Solids

2.1.1 The proposed decomposition

Following the developments of [7], as indicated in Fig. 1, we view the structure of a crystalline solid as an aggregate of volume elements, or *lattice blocks*. For the crystalline solid subjected to a deformation $\mathbf{F}$, three mechanisms are considered. Slip between lattice blocks may be activated (i.e. plastic flow), designated by $\mathbf{F^{Flow}}$, followed by lattice distortion $\mathbf{F^{Lattice}}$, which is a combination of both inelastic ($\mathbf{F^I}$) and elastic ($\mathbf{F}^e$) processes. Thus:

$$\mathbf{F} \equiv \mathbf{F^{Lattice}F^{Flow}}, \qquad\qquad (2.1.1)$$

This proposed decomposition is to provide a distinction between plastic *flow* ($\mathbf{F^{Flow}}$) and plastic *lattice-block distortions (* $\mathbf{F^I}$*)*arising due to a storage of dislocations in crystalline solids, cf. [14].

2.1.2 The Incompatibility of $\mathbf{F^{Flow}}$ *and* $\mathbf{F^{Lattice}}$

If, as shown in Fig. 2, glide occurs along multiple planes (as indicated by the red arrows), then small gaps, or displacement discontinuities, will arise between lattice blocks, resulting in a non-compact configuration [8]. The distortion $\mathbf{F^{Flow}}$ is thus generally *incompatible*, i.e. not compatible with the existence of a unique displacement field [8]. $\mathbf{F^{Lattice}}$, which maps from a non-compact configuration to the final configuration, is consequently also incompatible. As with

4

any continuum, however, it is required that the compact reference configuration be mapped by a compatible deformation $\mathbf{F}$ to a compact final configuration. Hence, $\mathbf{F^{Flow}}$ and $\mathbf{F^{Lattice}}$ must evolve in a consistent manner, such that their product $\mathbf{F^{Lattice}F^{Flow}}$ is compatible.

2.2 Compatibility and Conditions for Failure

In crystalline solids, the necessary and sufficient condition for compatible deformation is expressed by a *first-order differential Law* (cf. [8]),

$$Curl(F^{Lattice}F^{Flow}) = 0 \tag{2.2.1}$$

where we have used the relations $\mathbf{F} \equiv \mathbf{F^{Lattice}F^{Flow}}$ and $\nabla_X \mathbf{x} = \mathbf{F}$. Alternatively, we may express (2.2.1) as an *integral Law*, by application of Stokes' theorem (cf. [8]), yielding the vector

$$\delta \equiv \oiint_C \mathbf{F^{Lattice}F^{Flow}} \, \mathbf{dX} \tag{2.2.2}$$

where the condition $\delta = 0$ is needed for compatible deformations. Any non-zero value of δ would indicate crack nucleation (i.e. the initiation of a topological defect). A computationally simple criterion for crack nucleation can thus be defined as outlined in the following section.

2.3 Computational scheme for the criterion δ

Our implementation is intended for a finite element scheme. Deformation $\boldsymbol{F}$ is generally computed from the nodal displacements, *assuming* unique and differentiable displacement fields, which assumes it is compatible throughout the simulation, irrespective of the constitutive behavior evolving at the integration points. Therefore, we can rewrite δ as

$$\delta \equiv \oiint_C \left(\mathbf{F} - \mathbf{F^{Lattice}F^{Flow}} \right) \mathbf{dX} \tag{2.3.1}$$

The integrand in equation (2.3.1) becomes non-zero only when the decomposition $\mathbf{F^{Lattice}F^{Flow}}$ is not equal to $\mathbf{F}$, which means that the evolving physical mechanisms in the crystalline solid cannot meet the assumption of compatibility, and equality (2.1.1) ceases to

apply. For the present finite-element implementation (using element deletion, see section 2.4), we need only use the centroidal values of $\mathbf{F}$, $\mathbf{F}^{\mathbf{Lattice}}$ and $\mathbf{F}^{\mathbf{Flow}}$. As discussed in [7], we can thus simplify the δ-criterion by defining an equivalent scalar measure (δ_s) as

$$\delta_s \equiv \left\| \mathbf{F} - \mathbf{F}^{\mathbf{Lattice}} \mathbf{F}^{\mathbf{Flow}} \right\| \mathbf{L}_0^e . \qquad (2.3.2)$$

Where $\mathbf{L}_0^e$ is the initial element characteristic length. As we showed in [7], for metals subjected to large deformations we have $\mathbf{F}^{\mathbf{Lattice}} \cong \mathbf{R}^e \mathbf{F}^{\mathbf{l}}$ and $\mathbf{F}^{\mathbf{Flow}} = \mathbf{F}^{-\mathbf{l}} \mathbf{F}^{\mathbf{p}}$. The fracture criterion thus reduces to

$$\delta_s = \left\| \mathbf{R}^e (\mathbf{U}^e - \mathbf{1}) \mathbf{F}^{\mathbf{p}} \right\| \mathbf{L}_0^e . \qquad (2.3.3)$$

This criterion underscores that, for crystalline solids, imposing the large-deformation constraint of $\mathbf{U}^e \cong \mathbf{1}$ limiting elastic strains (thus the cohesive forces [8]) is sufficient to monitor the onset of fracture, once the constitutive law is defined. Note that $\mathbf{F}^{\mathbf{l}}$ does not appear in the calculation of δ_s; thus its computation is not needed for fracture prediction. For a further discussion of its relevance, and for a detailed account of how to calculate $\mathbf{F}^{\mathbf{l}}$, $\mathbf{F}^{e}$, and $\mathbf{F}^{\mathbf{Flow}}$ see [7].

2.4 Numerical Generation of Failure Surfaces

When the failure criterion (Eq. 2.3.3) is met, there are various finite-element techniques to treat the failed element, and to generate the corresponding failure surfaces. For instance, *interelement crack* methods [15, 16] could be used, which rely on node separation, and have been used in the modeling of the failure of heterogeneous structures, cf. [17]. However, the crack path would then be confined to element edges, which would not properly account for ductile crack profiles, such as with crack blunting; cf. the various smooth-blunting and blunting-to-vertices profiles observed experimentally in [18]. Moreover, when simulating fracture of microstructures at small length-scales, it would not be physically reasonable to require the crack-tip radius to be infinitesimal. We, therefore, use the *element removal* method combined with highly refined meshes, in order to better capture the crack tip profiles. Briefly, element removal

involves the deletion of an element's contribution to the global system of equations, by zeroing out the strains passed into the flagged element, and zeroing out the stresses passed out from it [19]. We note that the associated nodal masses are not correspondingly removed from the system of equations [20] unless the nodes are themselves removed (following the deletion of all elements sharing that node). This loss of mass is apparently non-physically based and could be a source of errors. However, with a sufficiently refined mesh, such a loss of mass is negligible. We, furthermore, note that the shape, size and orientation of elements generally introduce a mesh dependency of crack propagation. However, with a sufficiently refined uniform unstructured mesh, the predicted trends for crack paths are reproducible, and mesh sensitivity is less consequential.

In this implementation, an element is flagged for removal when the condition,

$$\delta_{Crit} / \mathrm{L}^c > 0.5, \tag{2.4.1}$$

is met; i.e. when the magnitude of the displacement incompatibility of deformation corresponds to half the current characteristic length (L^c) of any element. To avoid spurious mesh dependence on element size [20] we have scaled the element removal criterion by L^c.

To avoid numerical instabilities in the mesh arising from sudden the removal of an element, the element satisfying Eq. (2.4.1) is numerically unloaded prior to deletion over a relatively brief span of **500** increments (note that the typical simulation spans over two million increments). Unloading follows the recursive formula of

$$\sigma_{ij}^{n+1} = \xi \sigma_{ij}^n, \tag{2.4.2}$$

where σ_{ij} is the Cauchy stress tensor, $\xi < 1$ is an arbitrary factor related to the rate of unloading (which we set as: $\xi = 0.995$), and n is increment number.

3. Microstructural Modeling

3.1 Overview of the 2139-Al Microstructure

The crystalline plasticity constitutive formulation requires the identification of specific crystal structures, slip systems and material properties. We consider in this study Al–Cu–Mg–Ag (Mn, Fe) alloys, which have multiple secondary phases, spanning multiple length scales, as summarized in Fig. 3 for a 2139-T8 Al plate. Fig. 3 (a) shows the dark-field TEM image of nano-sized Al_2Cu precipitate platelets, Ω and θ' that are interspersed in the grains of the alloy. Fig. 3 (b) shows a bright-field image of micron sized Mn-bearing dispersoids (T-phase) and coarser Mn-bearing inclusions, also found in the microstructure. For more details on the characterization of microstructure see [21]. Fig. 3 (c) summarizes by schematic the different secondary phases and their associated length scales.

The different phases identified in Fig. 3 have different crystallographic properties. For an accurate description of their roles in the deformation of the microstructure, it is critical to account for these differences, as shown in Fig. 4. The θ' crystal has a tetragonal structure, $I\bar{4}m2$, with a=0.404 nm, c=0.58 nm [22] and whose slip systems have been determined by considering the densest planes and shortest burgers vectors, six of which are listed in Fig. 4. The generally accepted structure for the Ω phase is the orthorhombic structure (Fmmm) proposed in [23], with a=0.496 nm, b=0.858 nm and c=0.848 nm. In this study, however, the Ω phase has been modeled by the alternative I4/mcm structure [24, 25], which is only a slight perturbation of Fmmm, but is essentially identical to the θ crystal, with a=0.607 nm and c=0.487 nm [26], and whose slip systems have been identified experimentally [27, 28], which are listed in Fig. 4. The Mn-bearing dispersoid has been identified as orthorhombic, with a Bbmm structure [29, 30] or, differing by a rotation of the reference frame, as a Cmcm structure [31]. In this study we select Cmcm structure, and assign to the dispersoids the slip systems determined experimentally for Cmcm crystals [32], as represented in Fig.7.

3.2 Rate-dependent Crystalline Plasticity

Constitutive formulations for rate-dependent multiple-slip crystal plasticity, which are coupled to evolutionary equations for dislocation-densities, have been used. For a more detailed presentation of the presently used formulation see [7]. For a more general discussion of crystalline plasticity, the reader is referred to [33, 34] as an introduction and to [35] for a more comprehensive review.

Briefly, the velocity gradient is decomposed into a symmetric deformation rate tensor D_{ij} and an anti-symmetric spin tensor W_{ij}, which are then additively decomposed into elastic and plastic parts according to

$$D_{ij} = D_{ij}^* + D_{ij}^p, \quad W_{ij} = W_{ij}^* + W_{ij}^p. \tag{3.1}$$

The inelastic parts can be related to the crystallographic slip-rates as

$$D_{ij}^p = P_{ij}^\alpha \dot{\gamma}^\alpha, \quad W_{ij}^p = \omega_{ij}^\alpha \dot{\gamma}^\alpha, \tag{3.2}$$

where α is summed over all slip-systems, P_{ij}^α and ω_{ij}^α are components of the symmetric and skew-symmetric parts of the Schmid tensor in the current configuration. The rate-dependent slip formulation follows from the power-law relation defined in each slip system α as

$$\dot{\gamma}^{(\alpha)} = \dot{\gamma}_{ref}^{(\alpha)} \left(\frac{\tau^{(\alpha)}}{\tau_{ref}^{(\alpha)}} \right) \left(\frac{\left| \tau^{(\alpha)} \right|}{\tau_{ref}^{(\alpha)}} \right)^{1/m - 1}, \tag{3.3}$$

where $\dot{\gamma}_{ref}^{(\alpha)}$ is the reference shear slip-rate arising at a reference shear stress $\tau_{ref}^{(\alpha)}$, and m is the strain-rate sensitivity parameter. The shear stress $\tau^{(\alpha)}$ is solved for from a stiff system of ordinary differential equations, see [36] for details. The reference shear stress ($\tau_{ref}^{(\alpha)}$) is a modification of the classical form [37] that relates crystal strength to a square-root of the immobile dislocation-density (ρ_{im}), such that

$$\tau_{ref}^{(\alpha)} = \left(\tau_y^{(\alpha)} + \mu \sum_\beta a_{\alpha\beta} b^{(\beta)} \sqrt{\rho_{im}^{(\beta)}} \right) \left(\frac{T}{T_0} \right)^{-\xi}, \tag{3.4}$$

9

where $\tau_y^{(\alpha)}$ is the static yield stress on slip system (α), μ is the shear modulus, $b^{(\beta)}$ is the magnitude of the Burgers vector for slip system (β) and the coefficients $a_{\alpha\beta}$ are slip-system interaction coefficients of order 1, which can be calculated using the formula $a_{\alpha\beta}{=}2\left|P_{ij}^{\alpha}P_{ij}^{\beta}\right|$. T is the current temperature, T_0 the reference temperature, and ξ a thermal softening exponent.

The dislocation structure of a crystalline solid is in this formulation characterized by the total dislocation density $\rho^{(\alpha)}$. An additive decomposition into a mobile and an immobile dislocation density, $\rho_m^{(\alpha)}$ and $\rho_{im}^{(\alpha)}$ is assumed, as detailed in [7]. It is then assumed that the balance between generation and annihilation of dislocation densities is a function of strain, leading to the following coupled evolutionary equations [38] in slip system α

$$\dot{\rho}_m^{(\alpha)} = \left|\dot{\gamma}^{(\alpha)}\right|\left(\frac{g_{sour}}{b_{(\alpha)}^2}\frac{\rho_{im}^{(\alpha)}}{\rho_m^{(\alpha)}} - g_{minter}\rho_m^{(\alpha)}\exp\left[-\frac{\Delta H(T)}{kT}\right] - \frac{g_{immob}}{b_{(\alpha)}}\sqrt{\rho_{im}^{(\alpha)}}\right)$$

$$\dot{\rho}_{im}^{(\alpha)} = \left|\dot{\gamma}^{(\alpha)}\right|\left(-g_{recov}\rho_{im}^{(\alpha)}\exp\left[-\frac{\Delta H(T)}{kT}\right] + g_{minter}\rho_m^{(\alpha)}\exp\left[-\frac{\Delta H(T)}{kT}\right] + \frac{g_{immob}}{b_{(\alpha)}}\sqrt{\rho_{im}^{(\alpha)}}\right)$$

(3.5)

where $\Delta H(T)$ is the temperature dependent enthalpy of activation of plastic deformation, k is the Boltzmann constant, and g_{sour}, g_{minter}, g_{recov}, and g_{immob} are coefficients relating to active dislocation mechanisms in a crystalline solid, as discussed in [39].

3.3 Rational Orientation of Crystals

It is known that Ω and θ' crystals nucleate and grow along rational habit planes in the matrix, which results in a predetermined relationship between slip systems in these precipitates and the matrix. Hence, to impart the rational orientations of Ω and θ' with respect to the matrix, as developed in [26], the necessary transformations are as summarized in Fig. 5.

Briefly, slip systems for crystals are defined in fractional coordinates (Fig. 5 (a)). As precipitates are non-cubic, vectors defining slip-plane normals are not equivalent to their Miller indices, and normals are obtained by a reciprocal lattice construct [40]. Slip vectors are then

mapped from the precipitate system to the matrix space (Fig. 5 (b)). This is achieved by the basis transformation sequence $[M_{cart}^{\alpha^{*}}][M_{\Omega}^{cart}]$. We thus identify the rational orientation relations between the precipitates and the matrix (see [26]). These rational vectors define a transformation $[T_{\alpha^{*}}^{\alpha}]$ (Fig. 5 (c)). In general, Fig. 5 (d), another transformation $[M_{\alpha}^{cart}]$ may be needed to take the slip vectors from a non-cubic matrix space to a Cartesian space. Euler angles are then assigned to every grain for alignment with respect to the polycrystalline aggregate axes, defined as $[T_{cart}^{Poly}]$, as adapted from [41]. Finally, Fig. 5 (e), the polycrystalline aggregate is then aligned with the element frame by a transformation $[T_{Poly}^{elem}]$. For more details see [42].

4. Results: The Role of Secondary Phases in Dynamic Failure

4.1 The Model

The model size is 500 μm × 500 μm, as shown in Fig. 6. The Euler angles for the matrix crystal are consistent with rolled aluminum plates [43]. The model is subjected to a strain rate of 5,000 s^{-1}. In these simulations, however, we do not retain the nano-sized dimensions of the Ω and θ' precipitates and Mn-bearing dispersed particles (dispersoids) found in 2139-Al [44]; instead only their crystalline properties and morphologies were considerer, to study the role of crystallography. A more representative model of the multiscale nature of the microstructure is presented in section 5. Hence, in these simulations, the Ω crystals were taken as 40 μm × 1 μm, θ' as 32 μm × 3 μm, and the Mn-bearing dispersoids as 44 μm × 22 μm, thus preserving their experimentally observed aspect ratios [44]. The material properties used in this study are summarized in Table I. For non-dimensionalization, the following characteristic quantities were used: Young's modulus of the matrix (E), the elastic dilatational wave speed in the matrix (c), burgers vector in the matrix (b_v), and room temperature (T_{ref}). The non-dimensionalized quantities are listed in Table II.

We begin by investigating four models. Model 1 corresponds to a single crystal with only Ω and θ' precipitates at a ratio of 1:1, interspersed as a regular array throughout the matrix

crystal (Fig. 6 (a)). Model 2 corresponds to a crystal with Mn-bearing dispersoids, also arranged in an array spanning the matrix (Fig. 6 (b)). Model 3 corresponds to a single crystal with precipitates and dispersed particles (Fig. 6 (c)). Model 4 is similar to Model 3, but with a volume fraction of Mn-bearing dispersoids that has been reduced from 8% to 3.5%.

We also investigated failure in a single crystal with a pre-crack with different arrangements of dispersed particles and precipitates as shown in Figs. 7. Figs. 7 (a) corresponds to an array of Mn-bearing dispersoids and Figs. 7 (b) to an array of Ω and θ' precipitates ahead of the crack tip. The crack is modeled as an essentially sharp line of discontinuity; the crack tip radius is zero, corresponding to a single node, and the crack surfaces subtend the tolerance angle of 0.002°. Moreover, to ensure its dominance, the pre-crack spans half the model's width, as shown in the figure. Convergent meshes, in the sense discussed in section 2.4, containing at least 12,500 elements were used for the models in Fig. 6, and 9,000 elements for the models in Figs. 7; the elements were four-noded quadrilaterals with reduced integration and relax-stiffness hourglass control. The constitutive description and the compatibility-based fracture criterion (δ) were both implemented as FORTRAN subroutines within ABAQUS with MPI parallelization for domain decomposition.

4.2 Discussion of Results

4.2.1 Fracture with precipitates in the microstructure

Fig. 8 shows the stress-strain curves for Model 1 with Ω and θ' precipitates (Fig. 6 (a)) and for pure aluminum (i.e. matrix-only). The salient results from these curves are given in Table III. From Fig. 8 and Table III, it is seen that precipitates enhance alloy strength by a significant percentage, without reducing the strain at failure. However, at least at the macroscopic level, the tensile toughness is not affected.

To further understand these interrelated effects at the microstructural scale, we compare state variable evolution for Model 1 (Fig. 9) with that for the matrix-only (Fig. 10). As seen from

the figures, deformation is much more uniform for Model 1, in comparison with the pure matrix, which can be immediately seen by comparing the straightness of the left edges in both models. When there are no precipitates, the matrix necks at the lower left corner. Comparing lattice rotations (ψ_{12}°) between these two models (Fig. 9 (a) and Fig. 10 (a)), the precipitates Ω and θ' rotate with opposite senses, resulting in a symmetric and homogenized deformation mode. We also see that the precipitates harden (τ_{ref}) at higher values in comparison with the pure matrix (Fig. 9 (b) and Fig. 10 (b)). Hardening occurs as a result of the evolution of the immobile dislocation densities (ρ_{im}^{tot}) (Eq. 2.2.5). As seen from Fig. 9 (c) and Fig. 10 (c), the immobile densities for Model 1 are higher than for the pure matrix. The uniform precipitate distribution results in this uniform hardening, making an alloy with precipitates less susceptible to local deformation and necking, as reflected in the accumulated plastic shear slip (γ^{p}) (Fig. 9 (d) and 10 (d)). The maximum adiabatic temperature rise (ΔT) (Figs. 9 (e) and 10 (e)) is significantly lower with the precipitates (Model 1) in comparison with the pure matrix, which indicates that a microstructure with Ω and θ' precipitates is also significantly less susceptible to localized thermal softening.

From the curves in Fig. 8 we also see that the presence of Ω and θ' precipitates results in the rapid unloading of the stress, which indicates reduced dynamic damage tolerance (see Table III). Fig. 11 compares the accumulated plastic shear slip (γ^{p}) for pure-aluminum and Model 1 at the nominal strain of 25%. Without precipitates, the matrix deforms intensely around the advancing crack tip, as can be seen from the red contours ahead of the crack tips (Fig. 11 (a)), which allows for significant *crack blunting*. In contrast, for Model 1 (Fig. 11 (b)), the precipitates constrain matrix deformation by stiffening the overall microstructure, resulting in reduced plastic processes ahead of the crack tip for the dissipation of energy, thus deteriorating the dynamic damage tolerance of the microstructure.

4.2.2 Fracture with the addition of Mn-bearing particles to the microstructure

The effects of adding Mn-bearing dispersoids to a microstructure (as outlined in Figs. 6 (b-d)) are summarized Table IV. As seen from the curves in Fig. 12, the Mn-bearing dispersoids increase the strength of the alloy for all three cases (Models 2- 4). However, dispersoids have a negative effect on the maximum values for the normal stress (σ_{22}^{TS}), strain (ε^{TS}), and greatly decrease the tensile toughness, as seen in Table IV. The deterioration of the mechanical properties of the microstructure is due to the *void-sheet* mechanism [45, 46] from these coarse Mn-bearing dispersoids, which controls ductile failure [47-49]. Fig. 13 shows the accumulated plastic shear slip (γ^p) for Model 2. As seen from Fig. 13 (a), Mn-bearing particles nucleate voids at their peripheries, labeled 1-3, within a band of localized matrix shear (red). In Fig. 13 (b), the formation a void-sheet between these Mn-bearing dispersoids can be clearly seen, as well as the nucleation of more voids, labeled 4-5, in a new shear localization band. In Fig. 13 (c), the splitting of the void-sheets to form large cracks can be seen. Hence, it is clear that Mn-bearing particles result in this void-sheet mechanism, which evolves very rapidly in the microstructure, over a span of just 1 µs, and it reduces alloy tensile properties. Nonetheless, we can see from the slower rate of stress unloading for Models 2-4 (cf. Fig. 8 and Fig. 12) that dynamic damage tolerance is enhanced with Mn-bearing particles.

Now, to compare the three cases containing Mn-bearing particles see Figs. 14 – 16. As can be judged from the free boundary at the left edges (Figs. 15 – 16), adding Mn-bearing dispersoids to a microstructure containing precipitates did not significantly affect the overall uniformity of deformation,. However, with the larger volume fractions of Mn-bearing dispersoids there are more crack nucleation sites, and the cracks can more easily coalesce into a single dominant crack, which results in the deterioration in tensile behavior (Fig. 12). This is consistent with experimental observations for aluminum alloys [50].

Furthermore, for Models 2 – 4 (Figs. 14 – 16), the lattice rotations (ψ_{12}°) attain their maximum values at the interfaces between the matrix and the Mn-bearing particles. In Fig. 14,

we see that bands of lattice rotations (green) easily link up due to the close proximity of the dispersoids, and that the cracks tend to follow these (green) lattice reorientation bands. We further see for Models 2 – 4 (Figs. 14 – 16) that work hardening (τ_{ref}) is much larger for the matrix with the dispersoids in comparison for the matrix with only precipitates (Model 1, Fig. 10). This underscores how dispersoids contribute to the higher strength of the alloy, as indicated by the higher corresponding stress-strain curves in Fig. 12. The immobile dislocation densities (ρ_{im}^{tot}), summed over all slip systems, and the accumulated plastic shear slip (γ^p) inside the dispersoids (Figs. 14 – 16) do not evolve significantly during the simulation, which indicates that Mn-bearing crystals, unlike precipitates, are non-shearable, i.e. they behave elastically. Thus, failure occurs by dispersoid pullout from the matrix along the shorter ends, cf. Fig. 16. This is consistent with experimental observations of large Mn-bearing particles in aluminum alloys [50]. Moreover, the adiabatic temperature rise (ΔT) at the interface between the matrix and the Mn-bearing dispersoids for Models 2 – 4 is significantly larger than at the interface with precipitates (cf. Model 1, Fig. 10), which indicates that dispersoids render the microstructure more susceptible to localized adiabatic softening.

From Fig. 17 for Model 3, we can also note the different deformation and failure modes of the precipitates and dispersoids. First, we predict plastic buckling of θ' precipitates. This phenomenon has been observed experimentally [51], as well as predicted in our earlier work [52], and relates to θ' accommodating the deformation of the adjacent matrix, while not being aligned with slip directions of the matrix. On the other hand, Ω, whose broad face is aligned with the $(1\bar{1}1)_{Al}$ matrix slip plane, is predicted to elongate. Examining the rational orientation of Ω with respect to the matrix crystal, we found that there are two active Ω slip systems, $[001](\bar{1}10)_{\Omega}$ and $[111](\bar{1}10)_{\Omega}$, with plane normals coincident with the $(1\bar{1}1)_{Al}$ matrix plane; therefore, slip for these systems is fully directed along the Ω broad face, which explains the predicted elongation. We note, however, that Ω precipitates in our models are much coarser than in actual aluminum alloys, where they are only a few unit cells thick [23].

We can also see from Fig. 17 (Model 3) that precipitates deform heavily, when the adjacent matrix localizes, and are easily cut through by the crack. On the other hand, dispersed particles are not visibly deformed, and the crack does not cut through them, but instead works its way around them. It appears, therefore, that the crack propagation resistance is predominantly from the dispersoids. We explored this result further by running simulations for Models 5 & 6, with dominant pre-cracks, as shown in Fig. 7.

As seen from the curves in Fig. 18 and from Table V, Mn-bearing dispersoids have a much more favorable effect on all the mechanical behavior of the microstructure when there is a dominant pre-crack in the region. Clearly, no real alloy is free from flaws, and therefore, we conclude that it is necessary to have a certain amount of dispersed particles in the microstructure to resist the propagation of pre-cracks, as it is evident from our simulations that precipitates have shown no capability of resisting crack propagation, but actually seem to deteriorate the tensile behavior of the microstructure in the presence of the pre-crack (cf. Table V).

To understand this change in trend with respect to the models without a pre-crack, Fig. 19 – 21 show the deformed pre-cracked models (i.e. the pre-cracked pure matrix and Models 5 & 6) with their corresponding state variables. Our first prediction is that the crack paths are significantly different for the three pre-cracked models, reflecting different propagation mechanisms. For the pure matrix case (Fig. 19), the crack grows along what is essentially the plane of maximum shear, and branches towards the end of the model; one branch *arresting* and blunting (the top one), and the other branch forming a void-sheet. For the case with Ω and θ' precipitates (Model 5, Fig. 20), the crack is initially deflected vertically, away from the zone with precipitates, due to the general increase in strength of the microstructure with the precipitates ahead of the crack tip. As the crack grows, it turns back in the direction of maximum shear, and cuts through the precipitates on its path.

For the case of Mn-bearing dispersoids (Fig. 21, Model 6) the behavior is different. The single dispersoids ahead of the crack tip deflects the crack, making it grow vertically downward, where it is arrested, corresponding to the plateau in the stress-strain curve in Fig. 18. The

arrested crack then resumes its growth along the direction of maximum shear, as expected with

ductile cracks. As the crack grows, we see that it tracks its path in between the dispersed

particles; in fact, the crack branches around a dispersed particle (Fig. 21). From these predictions

it follows that Mn-bearing particles are capable of deflecting cracks, while the precipitates Ω and

θ' have not shown this ability.

Moreover, we predict for the Mn-bearing dispersoids (Model 6, Fig. 21) that the: lattice

rotations (ψ_{12}°), work hardening (τ_{ref}), total immobile dislocation densities (ρ_{im}^{tot}), accumulated

plastic shear slip (γ^{P}) and adiabatic temperature rise (ΔT), are more spread out than in either

Model 5 (Fig. 20) or in the pre-cracked pure aluminum matrix (Fig. 19). Hence, the Mn-bearing

particles promote plastic processes in the *entire* microstructural regions containing pre-cracks,

while precipitates *localize* plasticity to the immediate vicinity of the pre-cracks, thereby

deteriorating the microstructure's resistance to crack propagation.

Note that the basic crack propagation direction in all models was roughly upward, and

toward a direction roughly approximating the global direction of maximum shear. The basic

direction of cracking is strongly influenced by the Euler angles of the matrix grain with respect

to the loading axes, and its favorably aligned slip systems. In the next section, we show different

crack propagation paths, which are affected by slip system alignment and lattice rotation.

5. Polycrystalline Results

5.1 Computational Model

In this brief section, we focus on a different but more descriptive model of an actual

microstructure, to confirm the reproducibility of the basic physical trends and predictions made

in the previous section and to elucidate the role of grain orientations in affecting crack

propagation. The length scales of the precipitates and dispersed particles are here set farther apart

(two orders of magnitude apart in terms of the areas) to better represent the mismatch in their

actual sizes, and improve the model's description of the multiscale nature of the microstructure, as shown in Fig. 22. Precipitate sizes are thus modeled as 34nm × 1000nm, to better represent their actual aspect ratios, while Mn-bearing particles are modeled as 2μm × 3μm. The Mn-bearing particles are here modeled as ellipsoids, to understand how crack nucleation can occur at their interfaces. It is to be noted, however, that in actual microstructures, particulates could in general be faceted, rather than smooth ellipsoids. The model size is 30μm × 30μm, representing a seventeen -grain aluminum aggregate, whose Euler angles are consistent with rolled aluminum plates [7]with low angle boundaries (10-15° misorientation). Approximately, 400 Ω precipitates (2% by area), 400 θ' precipitates (2% by area) and nine Mn-bearing particles (4% by area) are interspersed in this model. Approximately 60,000 plane strain bi-linear (4-node) elements were used, with reduced integration and assumed-strain hourglass control, and approximately 5,000 elements per element. The model was subjected to a dynamic normal strain rate of 50,000 s^{-1}, consistent with impact loading conditions. The nominal strain at which calculations were terminated was 10%.

5.2 Discussion of the Results

As seen in Fig. 23, the accumulated plastic shear slip (γ^{pl}) localizes to form coarse slip bands (red) in the different grains, with local plastic strains accumulating in excess of 50% in the center of the bands. In particular, as seen in Figs. 23 (b-c), the slip patterns and the formation of slip bands depend on the local grain and its orientation with respect to the global axes, which determines the activation of slip along its different crystallographic systems. Fig. 24 summarizes across the seventeen grain aggregate the evolution of immobile dislocation densities, indicative of plastic slip activity under the dynamic load, along the twelve aluminum (FCC) slip systems. As can be seen from the plots, the grains activate different slip systems as a result of their local orientation relationships. Some slip systems are also seen to be active, thus favorably aligned, across multiple neighboring grains, a result of the small misorientation angles between grains.

Fig. 23 also indicates the nucleation and growth of primary crack (circled in yellow) and later a pair of secondary cracks (circled in black). Based on Figs. 25 (a-c), we can predict a first nucleation of the ductile crack, once again, at the Mn-bearing particle, followed by cracking of the matrix near the stiffening precipitates. Thus, low angle boundaries are not predicted to initiate cracks in the modeled microstructure. This result is consistent with fact that the crystallographic incompatibilities (thus incompatible slip activity) introduced at low angle boundaries (homophase interfaces) are smaller than at secondary phase boundaries (heterophase interfaces).

The primary crack grows roughly along the 45° direction of global maximum shear, in both directions of the grain, before turning roughly horizontal at either boundary of the grain. Hence, instead of the crack propagating across grains along its initial direction, the difference in plastic activity and crystallographic properties forces it to stop momentarily and change orientation. The incompatibility of deformation that naturally exists at the GBs promotes intergranular crack propagation. Thus, the resulting zigzag pattern of the fracture surface is a consequence of the local competition between evolving GB plasticity incompatibilities (see Fig. 24), and the 45° direction of maximum shear.

As the primary crack tip impinges on and crosses into the grain's right neighbor, we predict blunting, as seen in Fig. 25 (c-d). Figs 25 (d-f) are shaded according to plastic shear slip, and compare the profiles of the primary crack and the two secondary cracks at a nominal strain of 8.5%. Clearly, as the primary crack moves from one grain to another, a change in propagation direction must take place in order to match local slip directions. This change of crack direction at GBs in a ductile matrix is predicted to cause blunting, since the coarse slip band in the target grain is predicted to propagate the crack across its width, followed by extensive local plastic deformation (Fig 25 (d)), prior to the formation of new crack tip at a local orientation favorable to propagation. This predicted mechanism of blunting and crack tip profile as a result of intense plastic slip ahead of the crack, are consistent with the same experimentally observed blunting mechanisms of high strength alloys under quasi-static conditions [18]. Our results indicate that

low angle boundaries influence crack propagation direction by creating a multiplicity of potential slip orientations, and result in the associated blunting of cracks as they attempt to cross into neighboring grains. The ability of low-angle boundaries to change macroscopic ductility under large deformations is consistent with the findings of [53] in their analysis of lattice misorientations, and our present predictions confirm their influential role in dynamic fracture.

Note, however, that with element deletion the sharpest crack here modeled is approximately 50nm wide, corresponding to the average element width. The minimum width of the nucleated cracks is mesh dependent, and must clearly be selected smaller than the phenomenology of interest, which often requires highly refined meshes. Extensive local deformations result in highly distorted elements (cf Fig. 25 (d) at the blunted crack tip), which lead to numerical instabilities and thus limit the amount of plasticity that can be modeled prior to element deletion. Nevertheless, the sequence and pattern of failure are consistent with the basic physics pertaining to compatibility based microstructural and fracture modeling.

6. Conclusions

A dislocation-density crystalline plasticity and a recently developed fracture criterion have been used to investigate large deformation and dynamic failure modes in aluminum alloys with complex microstructures. The results indicate that precipitates can significantly improve the tensile strength and toughness in the absence of initial cracks or flaws. Once a crack nucleates, however, the precipitates are detrimental to the microstructure's dynamic damage tolerance. In contrast, dispersoids primarily contribute by promoting the dynamic damage tolerance, especially in a microstructure that has initial micro-cracks, by resisting crack propagation. Dispersoids, however, also nucleate cracks, reducing the tensile toughness of the alloy. They should therefore be distributed in low volume fractions, and well interspersed, to minimize interactions that lead to void-sheet formation. No alloy can be defect-free, especially in high strain rate applications, where damage is always expected in some regions of the microstructure,

thus the combination of Mn-bearing particles can be used to resist crack propagation, and Ω and θ' precipitates can be used to enhance strength and toughness. Furthermore, predictions indicate that low angle boundaries can change the propagation direction of ductile cracks, contributing to dynamic damage tolerance by activating a multiplicity of slip and crack propagation directions in the matrix. Low angle boundaries were not predicted to initiate cracks during the simulations; instead cracks nucleated at secondary phases, since heterophase interfaces are in this case associated with larger deformation incompatibilities than the homophase interfaces. Hence, distributions can be determined for optimal strength, toughness and dynamic damage tolerance.

References

1. Eschbach, L., C. Solenthaler, P.J. Uggowitzer, and M.O. Speidel, *Strength and Fracture Toughness of Spray Formed Al-Cu-Mg-Ag Alloys.* Materials Science and Technology, 1999. **15**(8): p. 926-932.
2. Polmear, I.J. and M.J. Couper, *Design and Development of an Experimental Wrought Aluminium-Alloy for Use at Elevated-Temperatures.* Metallurgical Transactions. A, Physical Metallurgy and Materials Science, 1988. **19**(4): p. 1027-1035.
3. Hono, K., N. Sano, S.S. Babu, R. Okano, and T. Sakurai, *Atom Probe Study of the Precipitation Process in Al-Cu-Mg-Ag Alloys.* Acta Metallurgica et Materialia, 1993. **41**(3): p. 829-838.
4. Howe, J.M. and D.P. Basile, *Minimum Detectable Solute Concentration in Atomic-Resolution Transmission Electron-Microscopy.* Acta Crystallographica. Section A, Foundations of Crystallography, 1988. **44**: p. 449.
5. Cho, A. and B. Bes, *Damage Tolerance Capability of an Al-Cu-Mg-Ag Alloy (2139).* Materials Science Forum, 2006. **519-521**: p. 603-08.
6. Elkhodary, K., W. Lee, L. Sun, D. Brenner, and M.A. Zikry, *Deformation Mechanisms of an Ω Precipitate in a High Strength Aluminum Alloy Subjected to High Strain Rates* Journal of Materials Research, 2010. **26**: p. 487-497.
7. Elkhodary, K.I. and M.A. Zikry, *A Fracture Criterion for Finitely Deforming Crystalline Solids -the Dynamic Fracture of Single Crystals.* Journal of the Mechanics and Physics of Solids, 2011. **59**: p. 2007-2022.
8. Kroner, E., *Continuum Theory of Defects*, in *Les Houches, Session XXXV,1980-Physics of Defects*, R. Balian and e. al., Editors. 1981, North-Holland: Amsterdam. p. 219-315.
9. Kroner, E., *Benefits and Shortcomings of the Continuous Theory of Dislocations.* International Journal of Solids and Structures, 2001. **38**: p. 1115-1134.
10. Miklashevich, I., *Micromechanics of Fracture in Generalized Spaces*2008, Amsterdam: Elsevier, Academic Press.
11. Crocker, A.G., P.E.J. Flewitt, and G.E. Smith, *Computational Modelling of Fracture in Polycrystalline Materials.* International Materials Review, 2005. **50**(2): p. 99-124.
12. Clayton, J.D., *Dynamic Plasticity and Fracture in High Density Polycrystals: Constitutive Modeling and Numerical Simulation.* Journal of Mechanics and Physics of Solids, 2005. **53**: p. 261-301.
13. Clayton, J.D., *Modeling Dynamic Plasticity and Spall Fracture in High Density Polycrystalline Alloys.* Int. J. Solids and Structures, 2005. **42**: p. 4613-4640.
14. Nemat-Nasser, S., *Plasticity. A Treatise on Finite Deformation of Heterogeneous Inelastic Materials*. Cambridge Monographs on Mechanics2009, Cambridge: Cambridge University Press.
15. Camacho, G.T. and M. Ortiz, *Computational Modelling of Impact damage in Brittle Materials.* International Journal of Solids and Structures, 1996. **33**(20-22): p. 2899-2938.
16. Xu, X.P. and A. Needleman, *Numerical Simulations of Fast Crack Growth in Brittle Solids.* Journal of the Mechanics and Physics of Solids, 1994. **42**(9): p. 1397-1434.

17. Chen, J., M. Crisfield, A.J. Kinloch, E.P. Busso, F.L. Matthews, and Y. Qiu, *Predicting Progressive Delamination of Composite Material Specimens via Interface Elements.* Mechanics of Composite Materials and Structures, 2010. **6**(4): p. 301-317.

18. Garrison, W.M. and K.J. Handerhan, *A Study of Crack Tip Blunting and the Influence of Blunting Behavior on the Fracture Toughness of Ultra-High Strength Steels.* Acta Metallurgica et Materialia, 1992. **40**(6): p. 1337-1355.

19. Hibbitt, Karlson, and Sorensen, *ABAQUS Analysis User's Manual*, 2007: Providence, RI.

20. Song, J.-H., H. Wnag, and T. Belytschko, *A Comparative Sutdy on Finite Element Methods for Dunamic Fracture.* Computational Mechanics, 2008. **42**: p. 239-250.

21. Lee, W. and M.A. Zikry, *Microstructural Characterization of a High Strength Aluminum.* Metallurgical and Materials Transactions A, 2011. **42**A: p. 1215-1221.

22. Silcock, J., T.J. Heal, and H.K. Hardy, *The Structural Ageing Characteristics of Ternary Aluminium-Copper Alloys with Cadmium, Indium or Tin.* Journal of the Institute of Metals, 1955. **84**(1): p. 23.

23. Knowles, K.M. and W.M. Stobbs, *The Structure of (111) Age-Hardening Precipitates in Al-Cu-Mg-Ag Alloys.* Acta Crystallographica. Section B, Structural Science, 1988. **44**: p. 207-227.

24. Garg, A. and J.M. Howe, *Convergent-Bean Electron-Diffraction Analysis of the Omega Phase in an AL-4.0 CU-0.5 MG-0.5 AG Alloy.* Acta Metallurgica et Materialia, 1991. **39**(8): p. 1939-1946.

25. Ringer, S. and K. Hono, *Microstructural Evolution and Age Hardening in Aluminium alloys: Atom Probe Field-Ion Microscopy and Transmission Electron Microscopy Studies.* Materials Characterization, 2000. **44**(1-2): p. 101-131.

26. Wang, S.C. and M.J. Starink, *Precipitates and Intermetallic Phases in Precipitation Hardening Al-Cu-Mg-(Li) Based Alloys.* International Materials Review, 2005. **50**: p. 193-215

27. Bonnet, R. and M. Loubradou, *Crystalline Defects in a BCT Al2Cu(Theta) Single Crystal Obtained by Unidirectional Solidification along [001].* Physica Status Solidi. A, Applied Research, 2002. **194**(1): p. 173-191.

28. Ignat, M. and F. Durand, *Deformation Lines on Al2Cu Single Crystals After Creep in Compression.* Scripta Metallurgica, 1976. **10**(7): p. 623-626.

29. Robinson, K., *The Unit Cell and Brillouin Zone of Ni4Mn11Al60 and Related Compounds.* Philosophical Magazine, 1952. **47**: p. 775-782.

30. Wang, S., L. Chunzhi, and Y. Minggao, *Determination of Structure of Al20Cu2Mn3 Phase in Al-Cu-Mn Alloys* Mat. Res. Bull., 1989. **24**: p. 1267-1270.

31. Mandolfo, L.F. Aluminum Alloys: Structure and Properties1976, London, UK: Butterworth.

32. Hildyard, R.C., D.J. Prior, D.R. Faulkner, and E. Mariani, *Microstructural Analysis of Anhydrite Rocks from the Triassic Evaporites, Umbria-Marche Apennines, Central Italy: An Insight into Deformation Mechanisms and Possible Slip Systems.* Journal of Structural Geology, 2009. **31**: p. 92-103.

33. Asaro, R.J., *Crystal Plasticity.* Journal of Applied Mechanics, 1983. **50**: p. 921-934.

34. Asaro, R.J. and J.R. Rice, *Strain Localization in Ductile Single Crystals.* Journal of Mechanics and Physics of Solids, 1977. **25**(5): p. 309-338.

35. Roters, F., P. Eisenlohr, L. Hantcherli, D.D. Tjahjanto, T.R. Bieler, and D. Raabe, *Overview of Constititutive Laws, Kinematics, Homogenization and Multiscale Methods in Crystal Plasticity Finite-Element Modeling: Theory, Experiments, Application.* Acta Materialia, 2010. **58**: p. 1152-1211.

36. Zikry, M., *An Accurate and Stable Algorithm for High Strain-Rate Finite Strain Plasticity.* Computers & Structures, 1994. **50**(3): p. 14.

37. Mughrabi, H., *A Tow Parameter Description of Heterogeneous Dislocation Distributions in Deformed Metal Crystals.* Materials Science Engineering, 1987. **85**: p. 15-31.

38. Ashmawi, W. and M. Zikry, *Prediction of Grain-Boundary Interfacial Mechanisms in Polycrystalline Materials.* Journal of Engineering Materials and Technology, 2002. **124**(1): p. 88-96.

39. Kameda, T. and M.A. Zikry, *Three Dimensional Dislocation-Based Crystalline Constitutive Formulation for ordered Intermetallics.* Scripta Materialia, 1996. **38**(4): p. 631-636.

40. Kelly, A., G.W. Groves, and P. Kidd, *Crystallography and Crystal Defects*2000, Chichester: John Wiley & Sons.

41. Randle, V., *The Measurement of Grain Boundary Geometry*, in *Electron Microscopy in Materials Science Series*1993, Institute of Physics Pub.: Bristol, UK

42. Elkhodary, K., L. Sun, D.L. Irving, D.W. Brenner, G. Ravichandran, and M.A. Zikry, *Integrated Experimental, Atomistic, and Microstructurally Based Finite Element Investigation of the Dynamic Compressive Behavior of 2139 Aluminum.* Journal of Applied Mechanics, 2009. **76**(5): p. 051306-1-9.

43. Polmear, I.J., *Light Alloys: From Traditional Alloys to Nanocrystals*. 4th Edition ed2006, Burlington, MA: Elsevier/ Butterworth-Heinemann. 153-154.

44. Elkhodary, K., W. Lee, L. Sun, D. Brenner, C. B., and M. Zikry. *Integrated Experimental and Computational Modeling of the High Strain-Rate Behavior of Aluminum Alloys.* in *Multiscale Polycrystal Mechanics of Complex Microstructures*. 2010. Boston, MA.

45. Reed-Hill, R.E., *Physical Metallurgy Principles*. University Series in Basic Engineering1973, New York: Van Nostrand.

46. Rogers, H.C., *The Tensile Fracture of Ductile Metals.* AIME Trans., 1960. **218**(3): p. 498-506.

47. Garrison, W.M. and N.R. Moody, *Ductile Fracture.* J. Phys. Chem. Solids, 1987. **48**(11): p. 1035-1074.

48. Knott, J.F. *Advances in Fracture Research*. in *7th Int. Conf. on Fracture*. 1989. Oxford, Pergamon.

49. Wilsdorf, H.G.F., *The Ductile Fracture of Metals: a Microstructural Viewpoint.* Mat. Sci. Eng., 1983. **59**: p. 1-39.

50. Walsh, J.A., K.V. Jata, and E.A. Starke Jr, *The influence of Mn Dispersoid Content and Stress State on Ductile Fracture of 2134 Type Al Alloys.* Acta Metallurgica, 1989. **37**(11): p. 2861-2871.

51. Embury, J., *Plastic-Flow in Dispersion Hardened Materials* Metallurgical Transactions A, Physical Metallurgy and Material Science, 1985. **16**(12): p. 2191-2200.

52. Elkhodary, K., W. Lee, B. Cheeseman, L.P. Sun, D.W. Brenner, and M.A. Zikry. *Deformation of Precipitate Platelets in High Strength Aluminum Alloys under High*

Strain-Rate Compression. in *The Vasek Vitek Honorary Symposium on Crystal Defects, Computational Materials Science and Applications.* 2010. Seattle, WA.

53.   Busso, E.P. and K.S. Cheong, *Effects of Lattice Misorientations on Strain Heterogeneities in FCC Polycrystals.* Journal of Mechanics and Physics of Solids, 2006. **54**: p. 671-689.

54.   Zhu, A.W., G.J. Shiflet, and E.A. Starke, *First Principles Calculations for Alloy Design of Moderate Temperature Age-Hardenable Al Alloys.* Materials Science Forum, 2006. **519-521**: p. 35-43.

55.   Smithells, C.J., *Smithells Metals Reference Book.* 8th ed. ASM International Metals Reference Book., ed. W.F. Gale and T.C. Totemeier. Vol. 1. 2004, Oxford [England] ; Burlington, MA: Elsevier Butterworth-Heinemann.

56.   Ali, A.A., G.N. Podus, and A.F. Sirenko, *Determining the Thermal Activation Parameters of Plastic Deformation of Metals from Data on the Kinetics of Creep and Relaxation of Mechanical Stresses.* Strength of Materials, 1979. **11**(5): p. 496.

57.   Zikry, M. and M. Kao, *Inelastic Microstructural Failure Modes in Crystalline Materials: The Σ33A and Σ11 High Angle Grain Boundaries.* International Journal of Plasticity, 1997. **13**(4): p. 31.

Tables and Figures

Table I: Material properties for FCC (Al), I4/mcm (Ω and θ') crystals

Property	Description	Value Al matrix	Value Ω, θ', Mn-Disp	Ref.
E (GPa)	Young's modulus	69	140	[54]
ν	Poisson's ratio	0.34	0.34	[54]
τ_y (MPa)	Static yield stress	35	35	---
ρ (g/cm^3)	Mass density (obtained from unit cell calculations)	2.70	4.36	---
Cp (J/kgK)	Specific heat (using the Neumann-Kopp rule for Ω, θ')	902	623	[55]
ΔH/k (K)	Activation enthalpy/ Boltzmann constant (Taking a mass weighted average for Ω, θ')	2500	3100	[56]
$\dot{\gamma}_{ref}$ (s^{-1})	Reference strain rate	0.001	0.001	[57]
ρ_{im}^0 (m^{-2})	Initial immobile dislocation density	10^{12}	10^8	---
ρ_m^0 (m^{-2})	Initial mobile dislocation density	10^{10}	10^6	---
T_0 (K)	Reference temperature	293	293	---
m	Strain rate sensitivity	0.02	0.02	[36]
g_{source}	Dislocation source coefficient	2.76E-5	2.76E-5	[57]
g_{immob}	Dislocation immobilization coefficient	0.0127	0.0127	[57]
g_{minter}	Mobile dislocation interaction coefficient	5.53E+4	5.53E+4	[57]
g_{recov}	Recovery coefficient	6.69E+5	6.69E+5	[57]
ξ	Thermal softening exponent	0.5	0.5	[36]
χ	Fraction of plastic dissipation to heat	0.9	0.9	[36]

Table II: Non-dimensionalization scheme for dynamic finite element analysis

Dimensional Quantity	Non-Dimensional Quantity (*)	Dimensional Quantity	Non-Dimensional Quantity (*)
Temperature (T)	$T* = \dfrac{T}{T_0}$	Stresses (τ, σ)	$(\tau*, \sigma*) = (\dfrac{\tau}{E}, \dfrac{\sigma}{E})$
Length (x)	$x* = \dfrac{x}{b_v}$	Strain Rate ($\dot{\gamma}$)	$\dot{\gamma}^* = \dot{\gamma}\dfrac{b_v}{c}$
Time (t)	$t* = t\dfrac{c}{b_v}$	Dislocation Density (ρ)	$\rho^* = \rho b_v^2$
Mass Density (ρ_{mass})	$\rho_{mass}^* = \rho_{mass}\dfrac{c^2}{E}$	Specific Heat (C_p)	$C_p^* = C_p\dfrac{T}{c^2}$

Table III: Mechanical Properties for the Matrix and the Matrix with Ω and θ'. The damage tolerances descriptions are only qualitative and relative to the other models.

Mechanical Property	Ω & θ' (Model 1)	Pure Matrix
Maximum tensile strength, σ^{TS} (MPa)	569	488
Corresponding nominal strain, ε^{TS} (%)	22.8	22.8
Tensile Toughness (MJ/m^3)	59.8	~59
Dynamic Damage Tolerance	Very Poor	Very Good

Table IV: Mechanical Properties after addition of Mn-bearing dispersoids. The damage tolerances descriptions are only qualitative and relative to the other models.

Mechanical Property	7.7%Dispersoids (Model 2)	7.7% Dispersoids, 3.5% Ω & θ' (Model 3)	3.5% Dispersoids, 3.5% Ω & θ' (Model 4)
σ^{TS} (MPa)	447	466	484
ε^{TS} (%)	15.9	11.9	14.4
Tensile Toughness (MJ/m^3)	~37	29.592	38.470
Dynamic Damage Tolerance	Good	Poor	Very Good

Table V: Mechanical Properties with a Dominant Pre-crack, models 5 & 6. The damage tolerances descriptions are only qualitative and relative to the other models.

Mechanical Property	Pure Matrix	Ω & θ' (Model 5)	Dispersoids (Model 6)
σ^{TS} (MPa)	196	192	239
ε^{TS} (%)	12.2	6.4	16.8
Tensile Toughness (MJ/m^3)	35.08	17.86	49.52
Dynamic Damage Tolerance	Good	Very poor	Very good
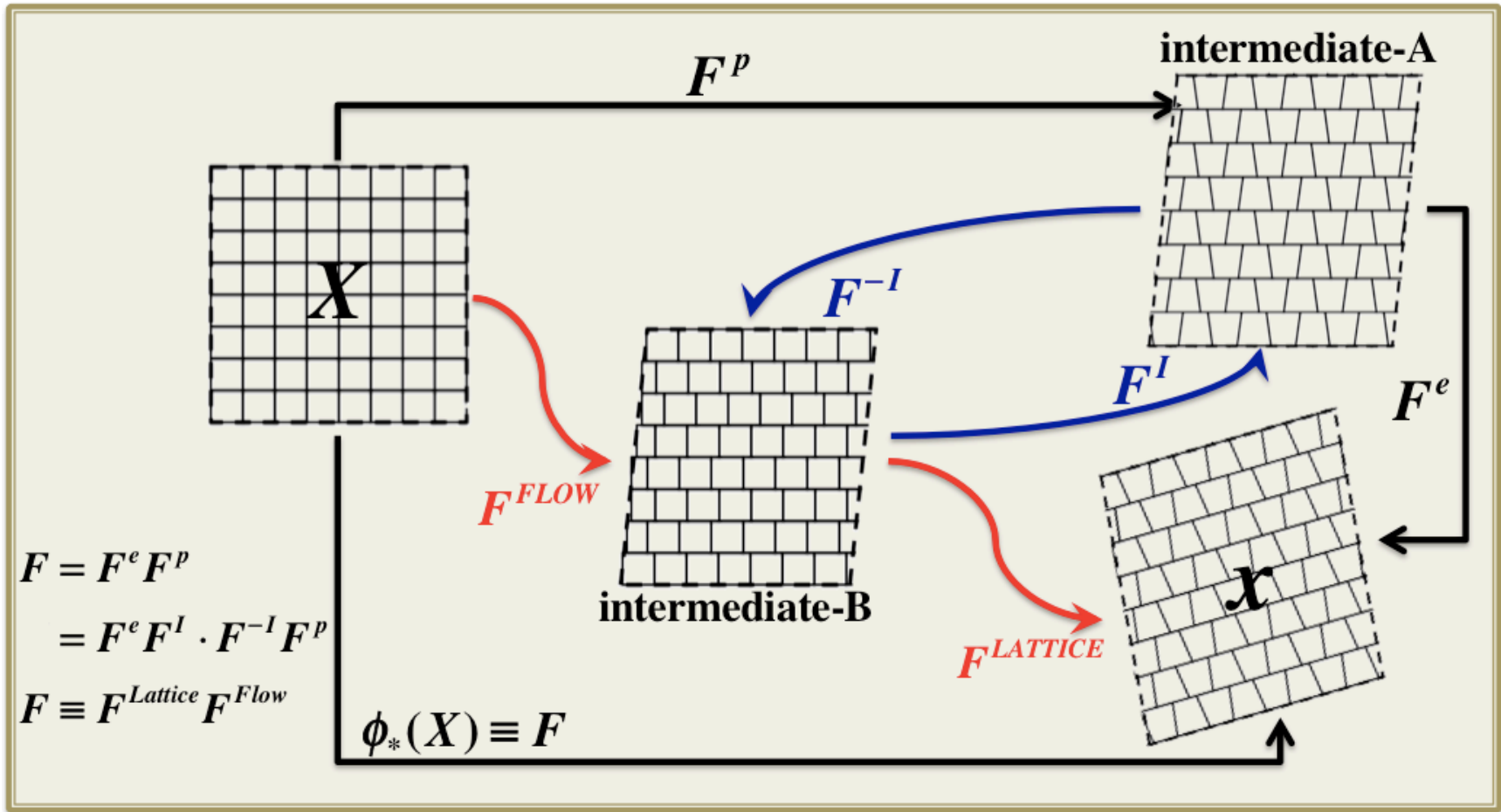
Figure 1: Proposed decomposition of the deformation gradient F

$F^{p} = F^{I}F^{Flow}$
(Incompatible)

non-compact

F^{e} (Incompatible)

Holes open up

compact

F
(compatible)
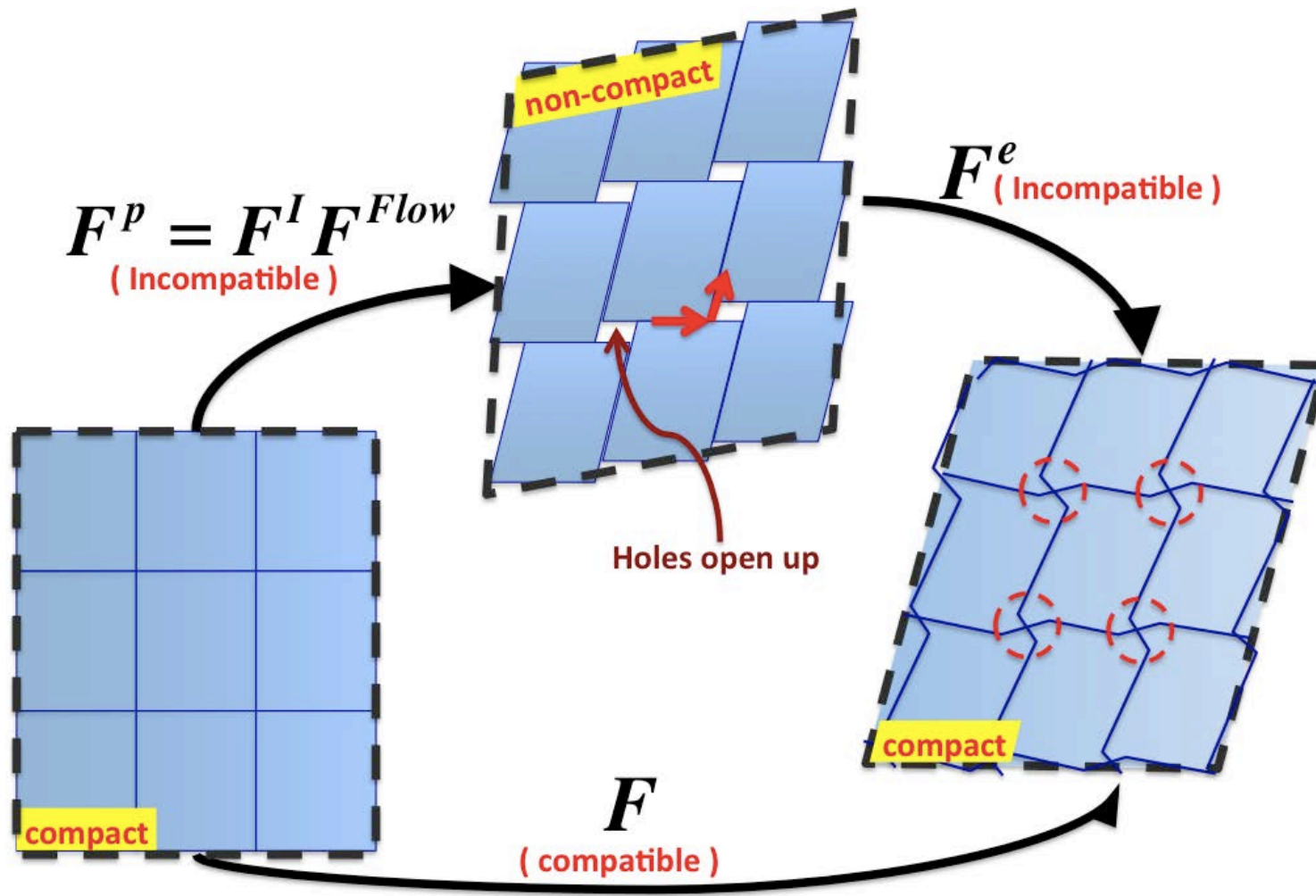
compact

Figure 2: Compact configurations and compatible distortions
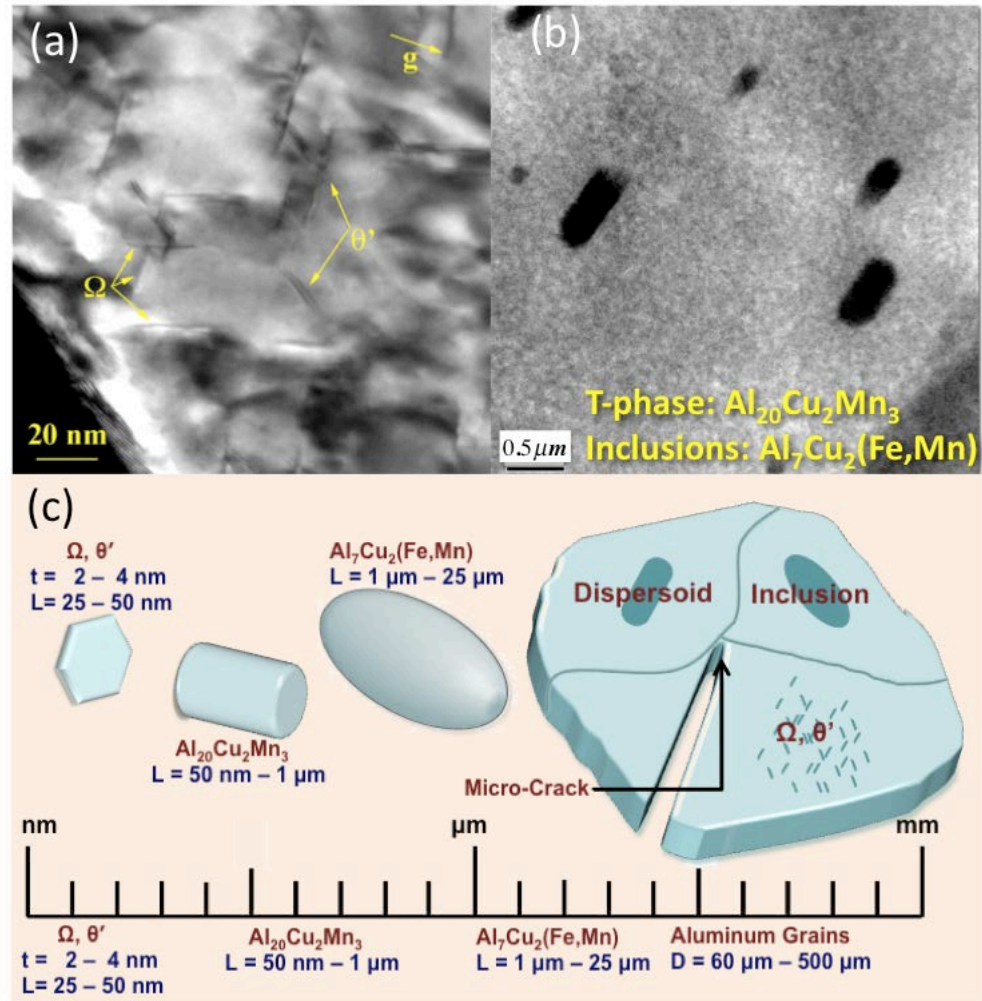
Figure 3: Al-Cu-Mg-Ag microstructure and corresponding length scales

Cmcm: Al$_{20}$Cu$_2$Mn$_3$ (Dispersoid)

ρ= 3.58g/cm^3
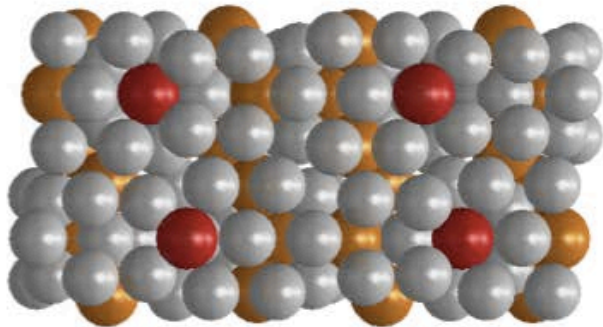
(1 0 0) [0 0 1]	Bv = 0.6993
(2 0 1) [1 $\bar{1}$ $\bar{2}$]	Bv = 1.6839
(2 0 1) [1 1 $\bar{2}$]	Bv = 1.6839

I4/mcm: Ω (Precipitate)

ρ= 4.36g/cm^3
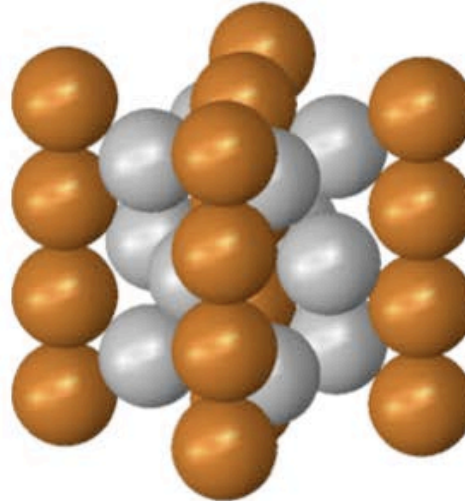
(1 1 0) [0 0 1]	Bv = 0.4931
($\bar{1}$ 1 0) [1 1 1]	Bv = 0.4931
(2 0 0) [0 0 1]	Bv = 0.6063
(1 1 2) [$\bar{1}$ $\bar{1}$ 1]	Bv = 0.6063
(0 1 1) [1 0 0]	Bv = 0.7778
(1 0 1) [0 1 0]	Bv = 0.7778

I$\bar{4}$m2: θ' (Precipitate)

ρ= 4.12g/cm^3
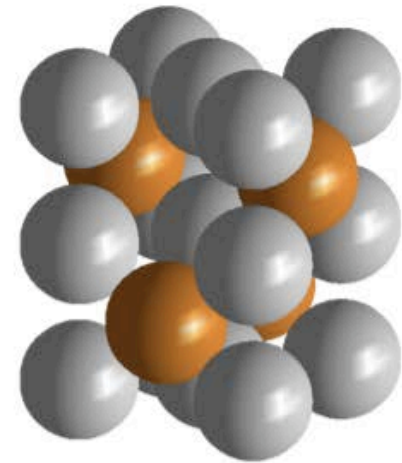
(0 0 1) [1 1 0]	Bv = 0.2857
(1 1 0) [1 $\bar{1}$ 0]	Bv = 0.2857
(1 1 0) [0 0 1]	Bv = 0.2900
(1 1 2) [$\bar{1}$ $\bar{1}$ 1]	Bv = 0.2857
(1 0 0) [0 0 1]	Bv = 0.2900
(1 1 0) [1 1 1]	Bv = 0.4071

Figure 4: Crystal structures and crystallographic properties of secondary phases in Al-Cu-Mg-Ag microstructures
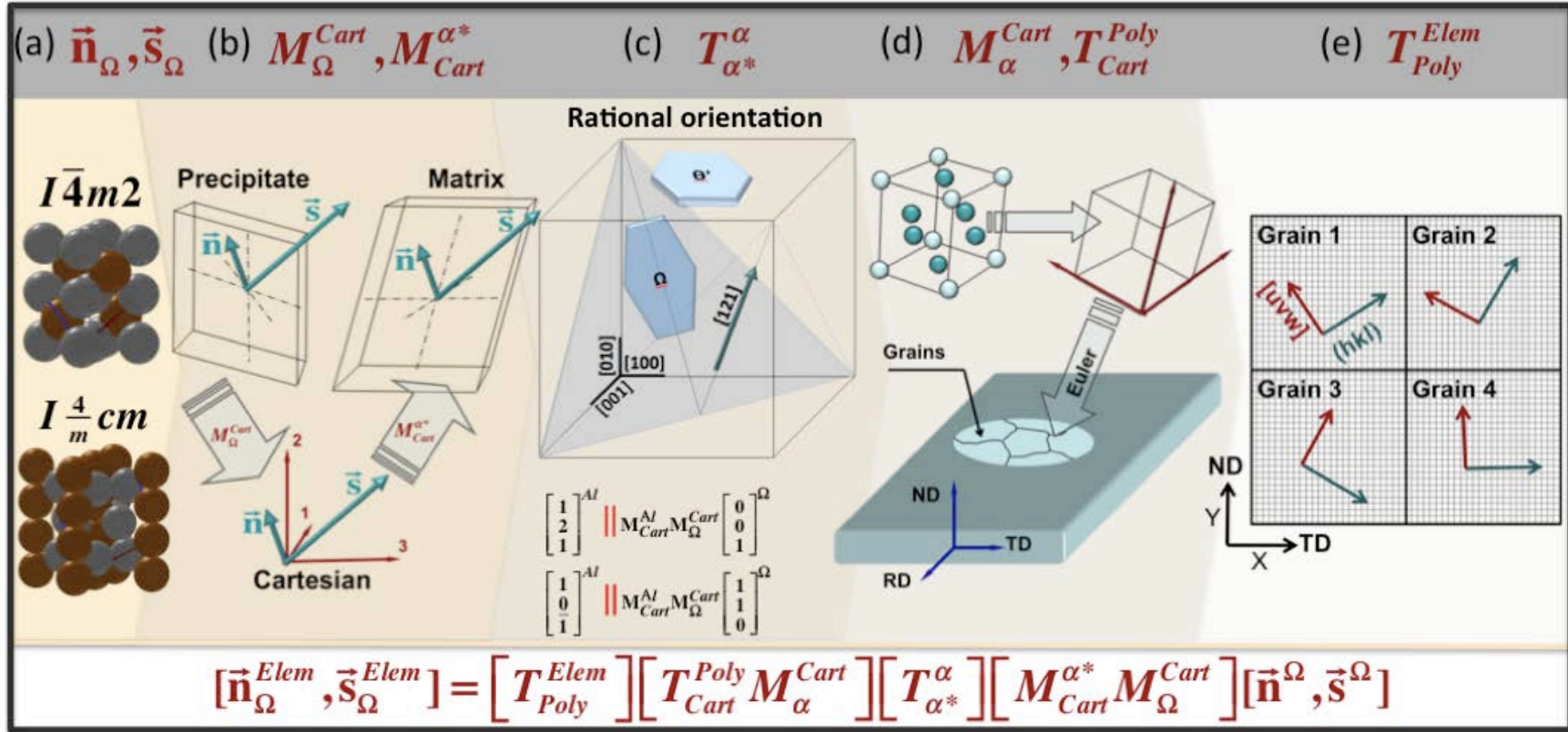
Figure 5: Rational orientation transformation sequence
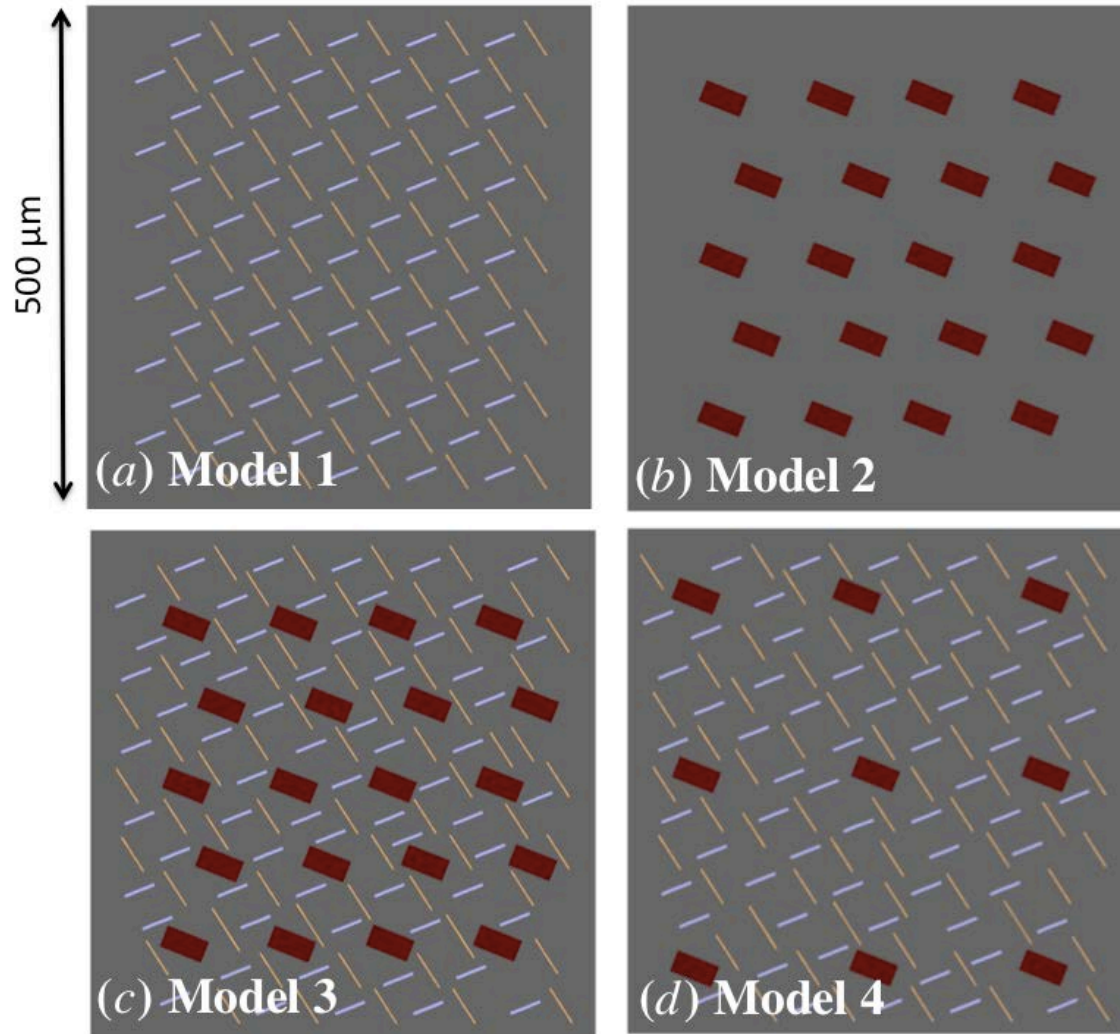
Figure 6: Four models of the microstructure, without a pre-crack. Light blue corresponds to coarse θ' precipitates, light orange corresponds to coarse Ω precipitates brick-red corresponds to coarse Mn-bearing particles.
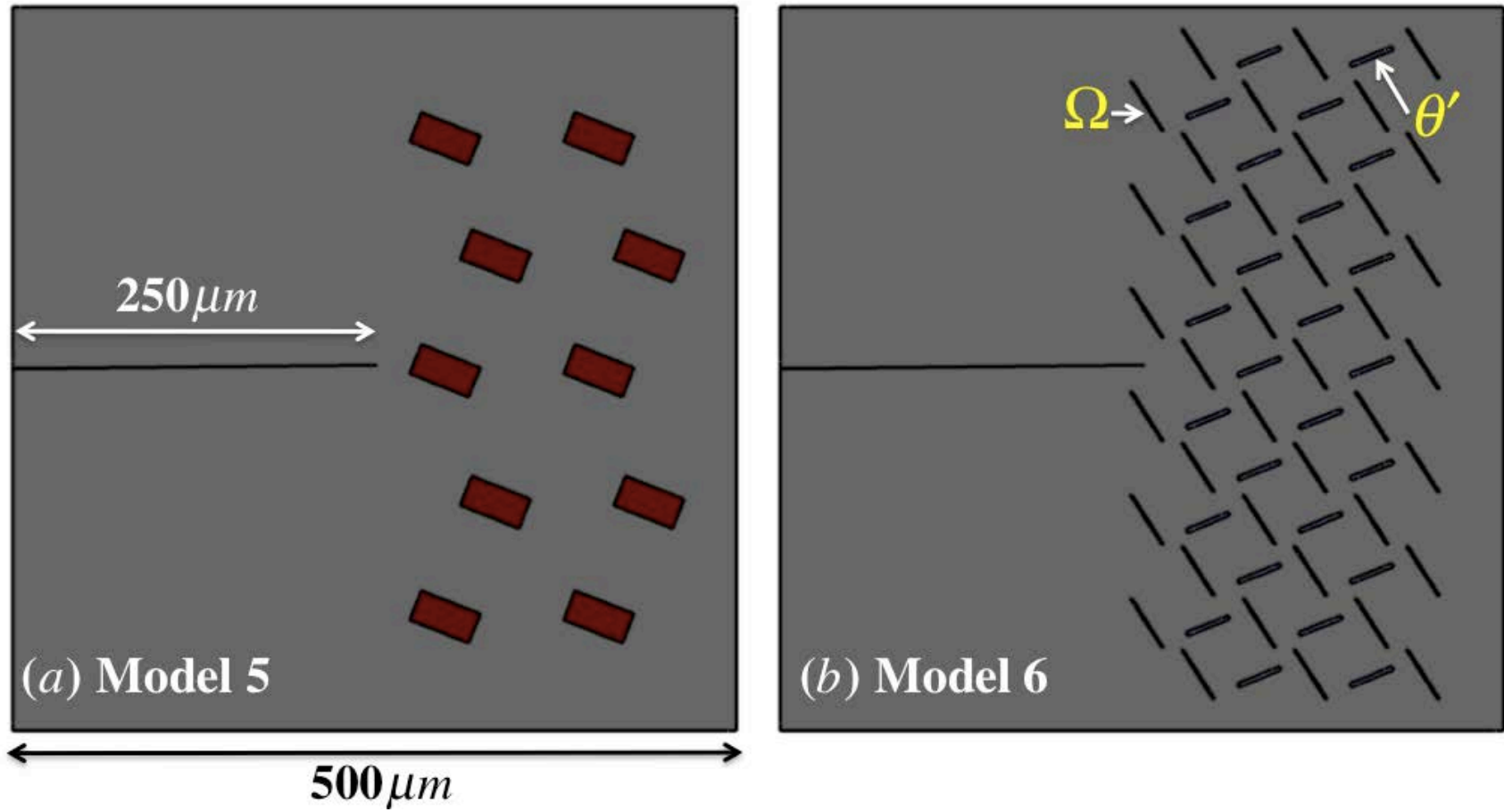
Figure 7: Two models of a pre-cracked microstructure. (a) with coarse Mn-bearing particles, (b) with Ω and θ' precipitates
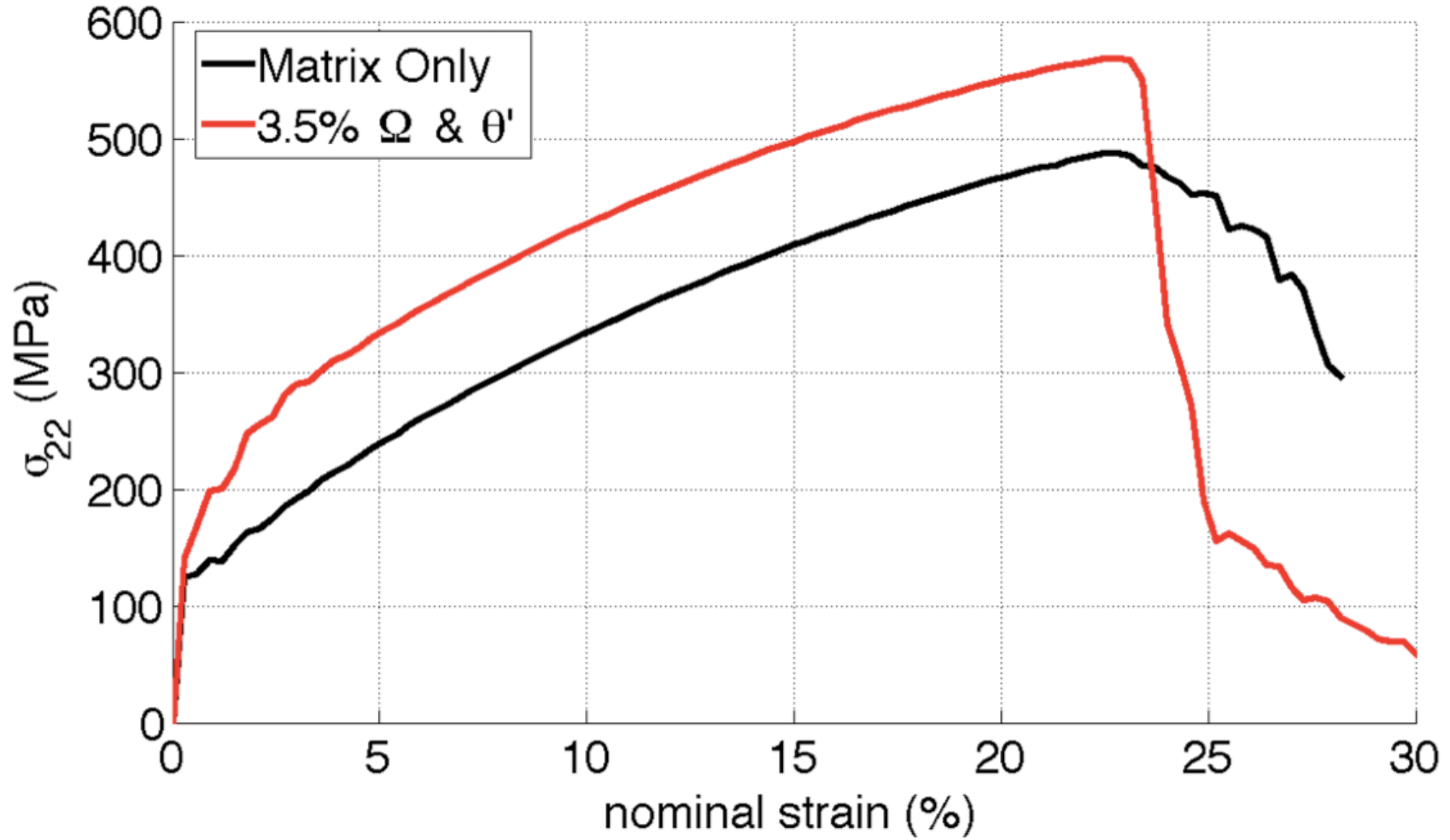
Figure 8: Stress-strain comparison of pure matrix and matrix with Ω and θ'. The earlier termination of the simulation for the pure matrix is as a result of excessive element distortion.

Model : Pure Matrix

(a) ψ°_{12} -0.5 1.6 3.7 5.8 7.8 9.9 12.0

(b) $\dfrac{\tau_{ref}}{E}$ 9.5E-04 1.8E-03 2.6E-03

(c) ρ^{tot}_{im} 1.1E+13 9.6E+13 1.9E+14

(d) γ^{pl} 0.1 0.2 0.3 0.5 0.6 0.8 1.3

(e) $\dfrac{\Delta T}{T_0}$ 0.03 0.23 0.43 0.64 0.84
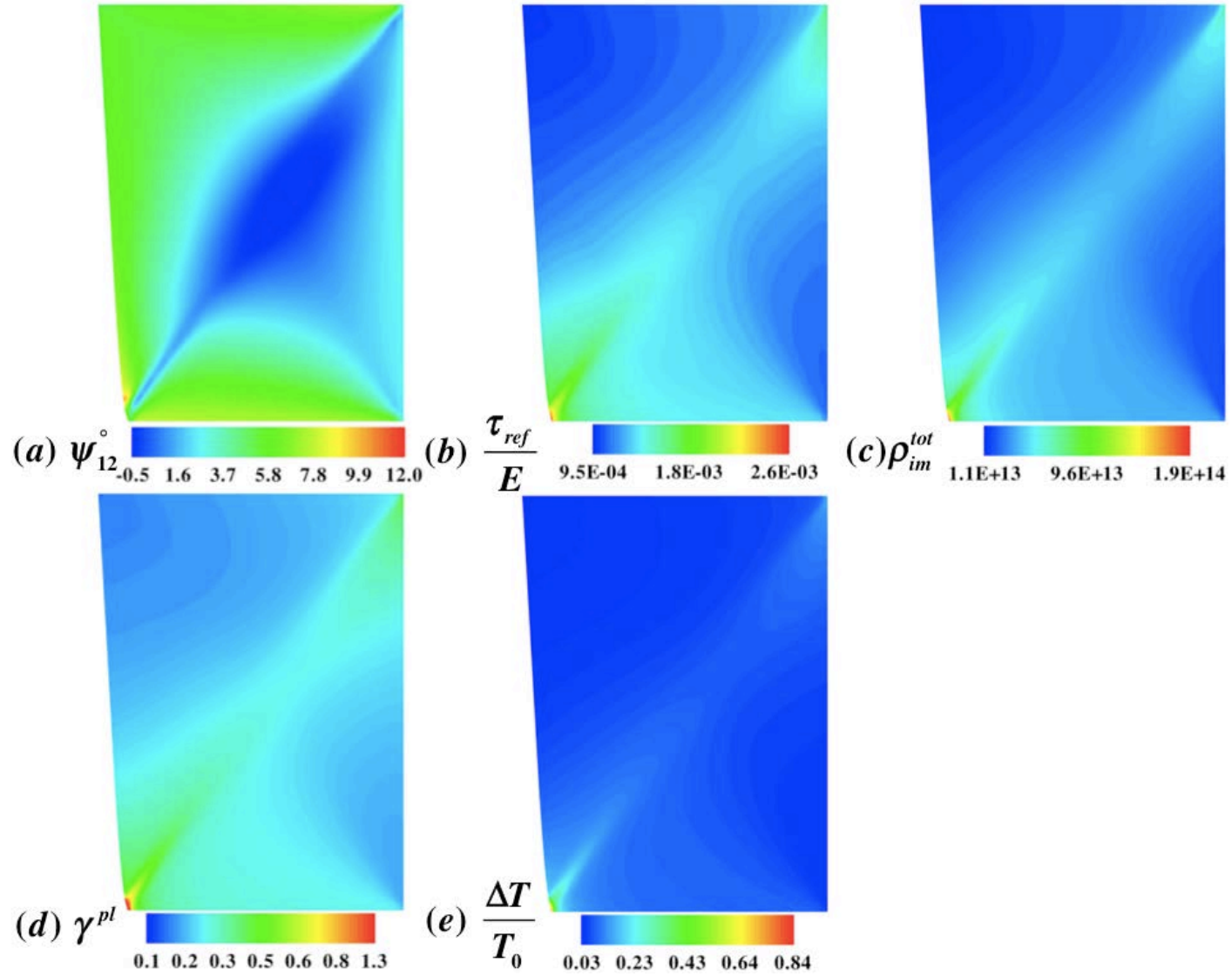
Figure 9: State variables for pure matrix at the nominal strain of 22.8%
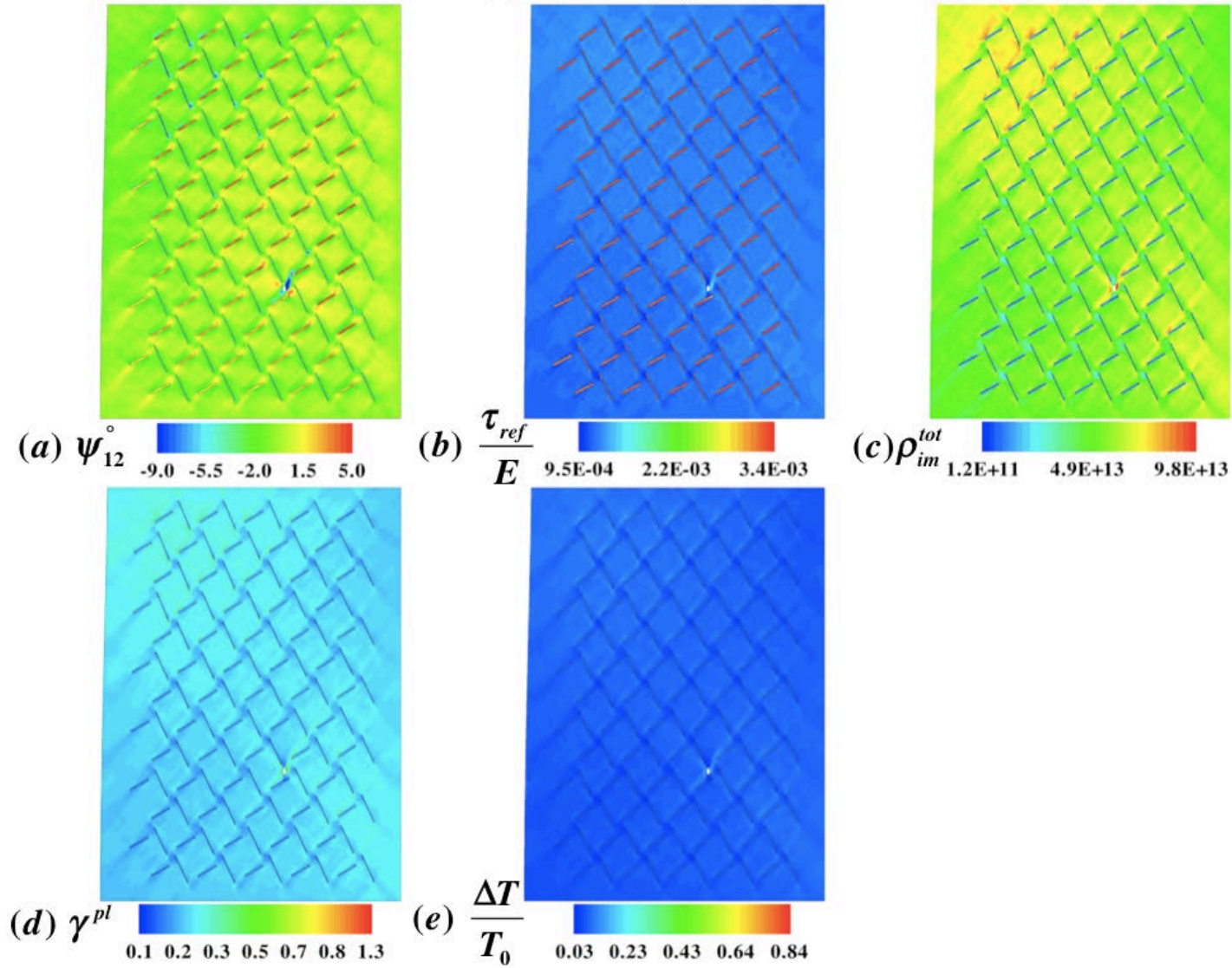
Figure 10: State variables of microstructure with Ω and θ' precipitates at the nominal strain of 22.8%

$(a)\ \gamma^{pl}$, MATRIX

$(b)\ \gamma^{pl}$, Ω & θ'
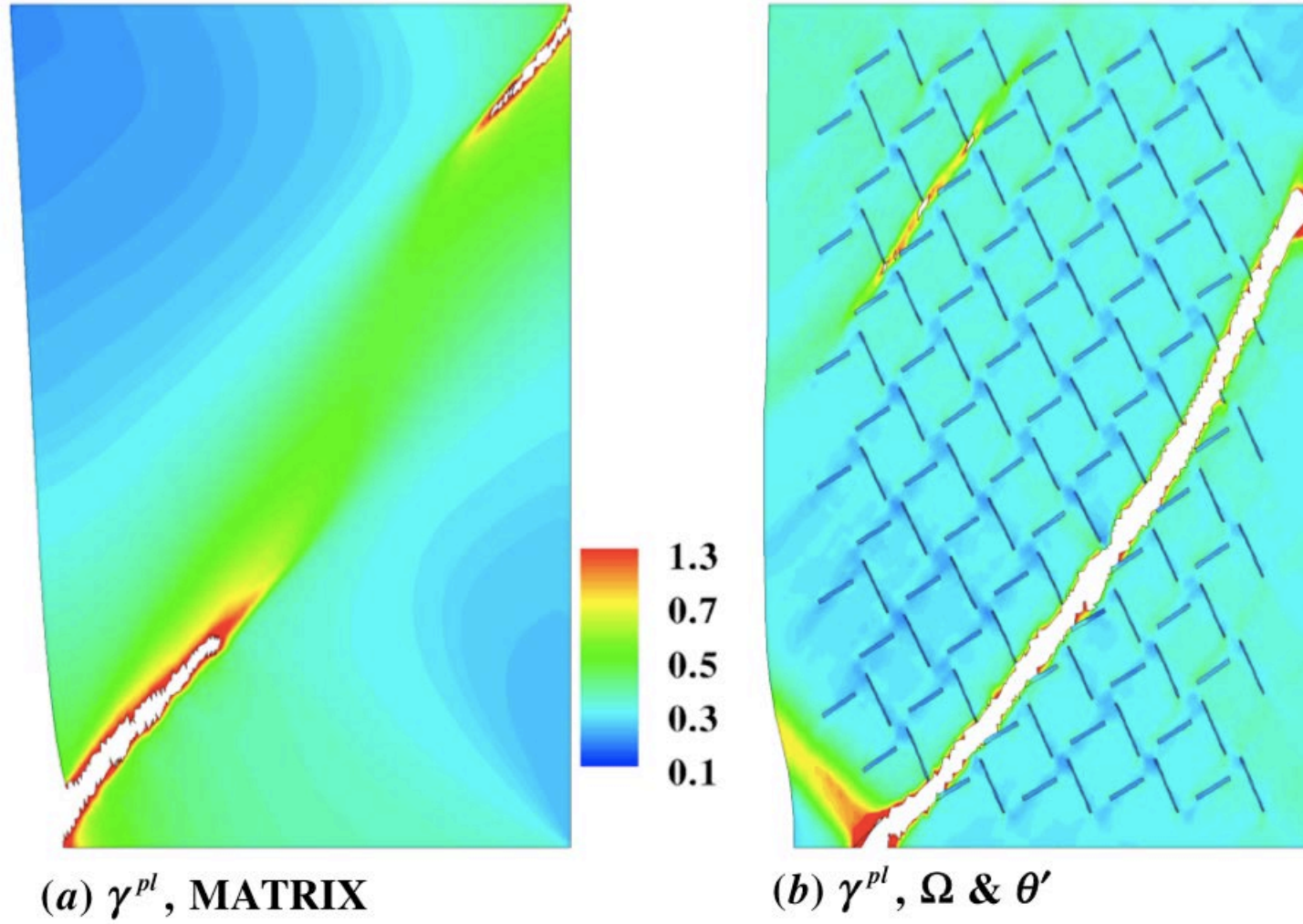
Figure 11: Comparison of the accumulated plastic shear slip for the pure matrix and model 1 at 25%

39
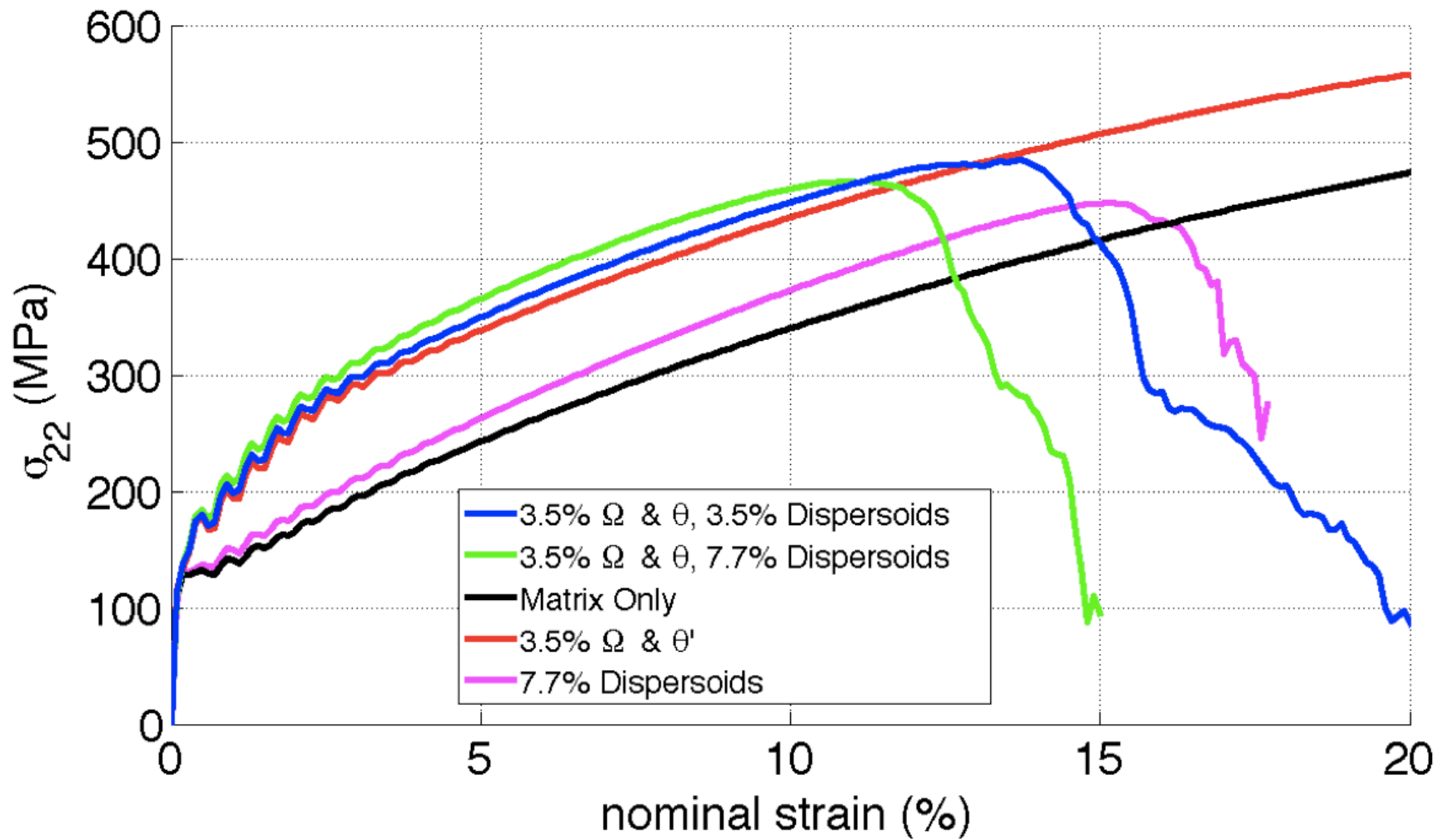
Figure 12: **Stress-strain behavior with coarse Mn-bearing particles in the microstructure. The earlier termination of the simulation for 7.7% Dispersoids is as a result of excessive element distortion.**
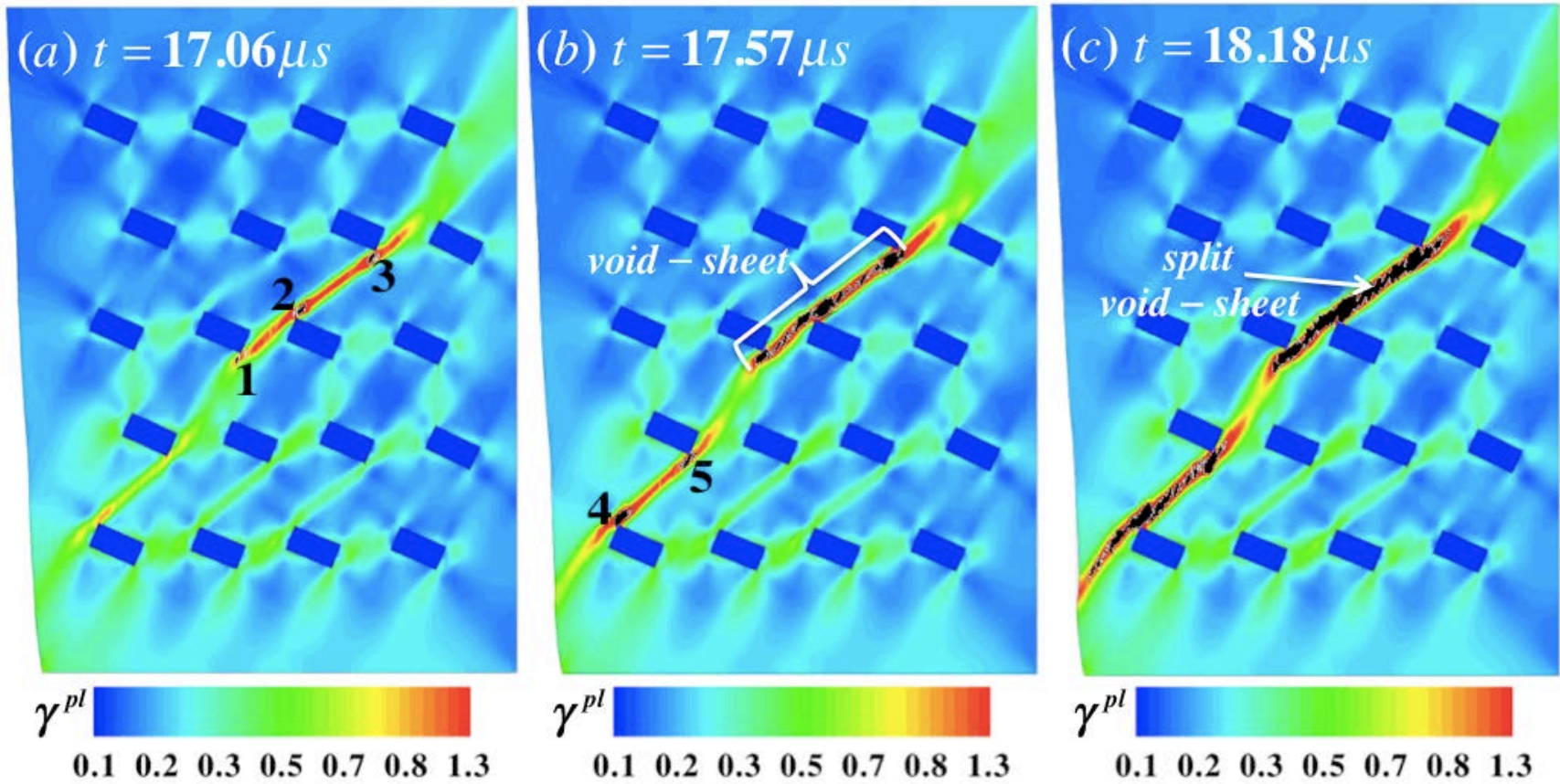
Figure 13: **The void-sheet mechanism of ductile fracture, driven by Mn-bearing dispersed particles**
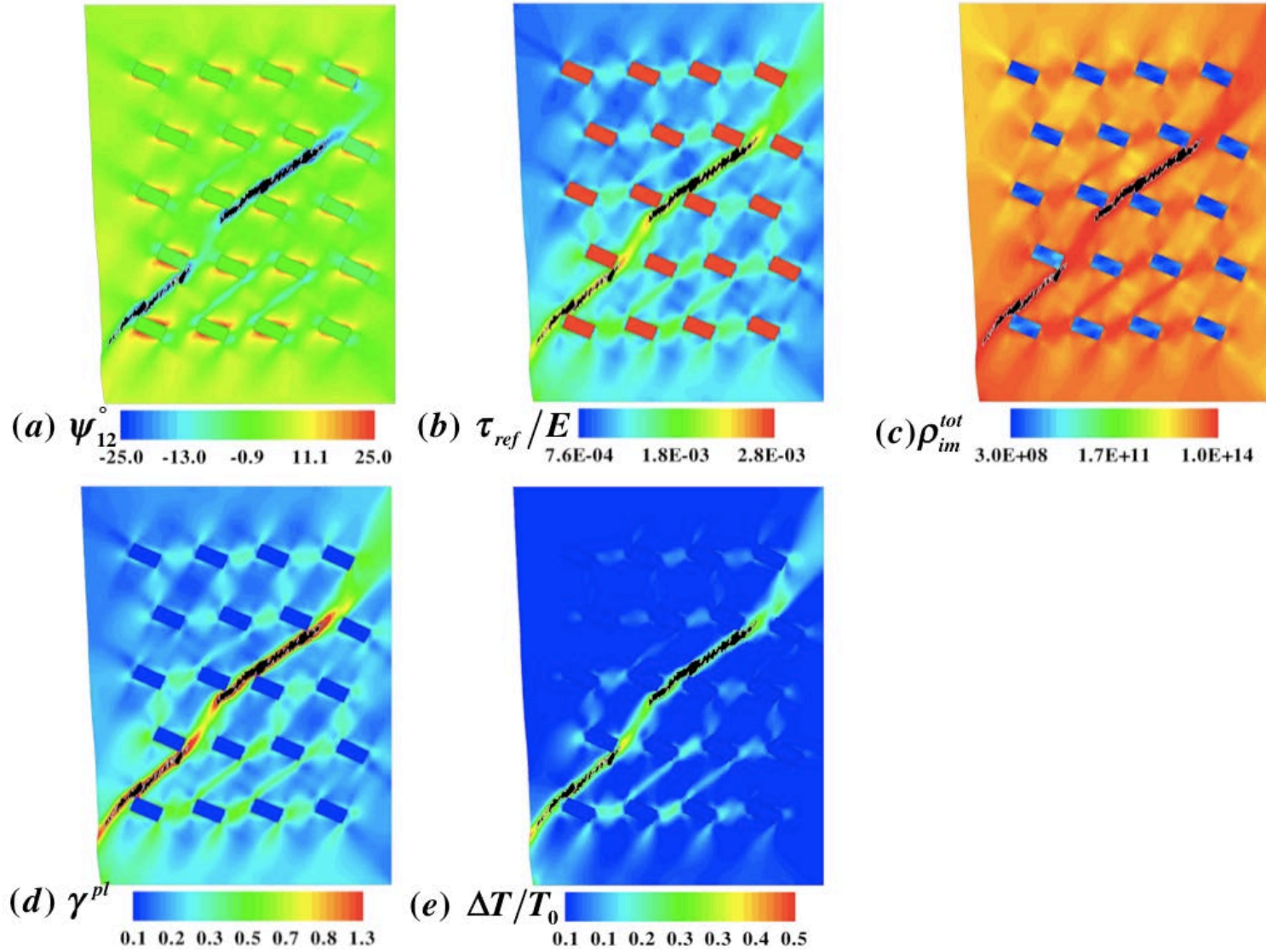
Figure 14: State variables for ruptured microstructure with Mn-bearing particles only (model 2)
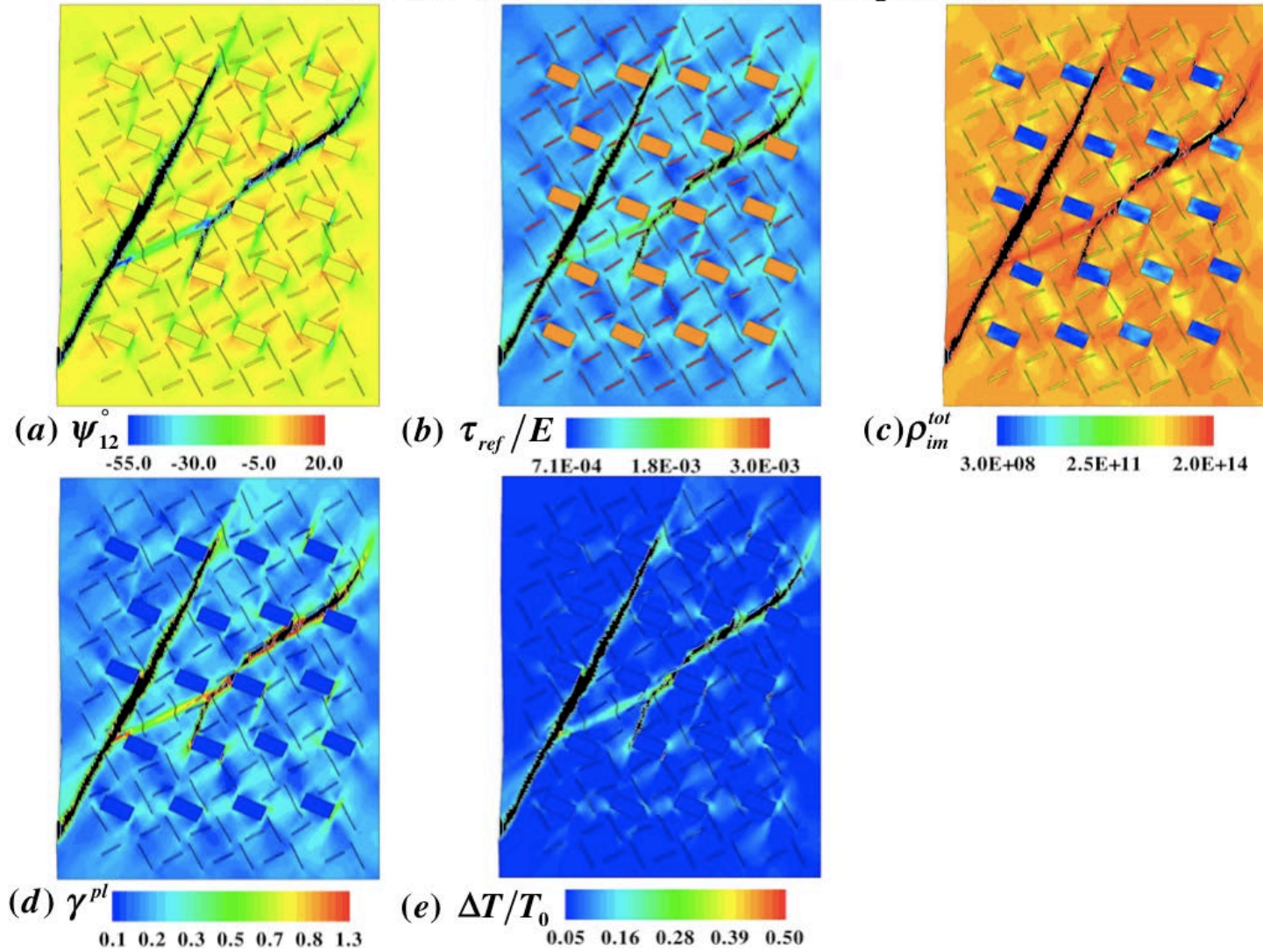
Figure 15: State variables for ruptured microstructure with 7.7% Mn-bearing particles and 3.5% Ω and θ' precipitates (Model 3)
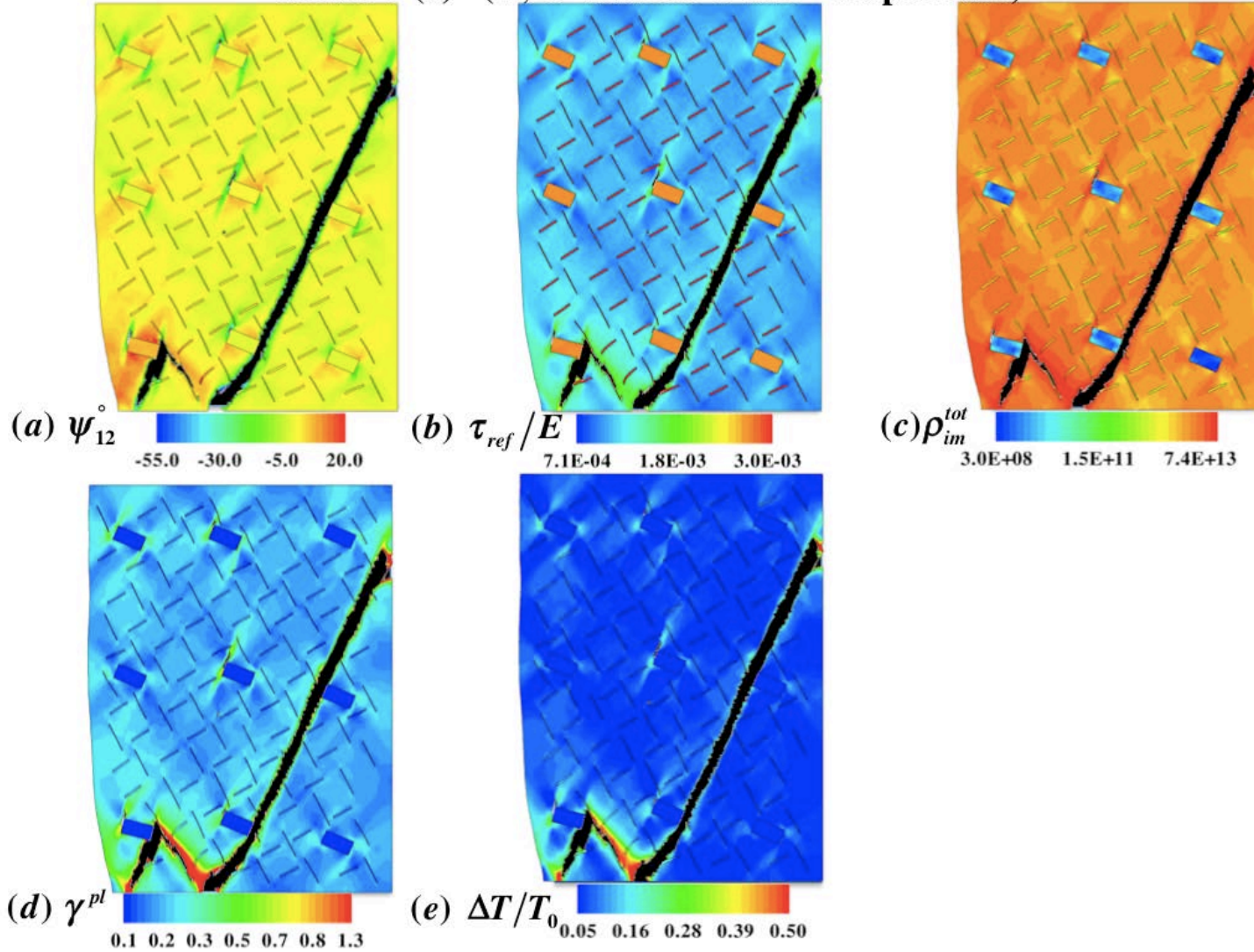
Figure 16: State variables for ruptured microstructure with 3.5% Mn-bearing particles and 3.5% Ω and θ' precipitates (Model 4)
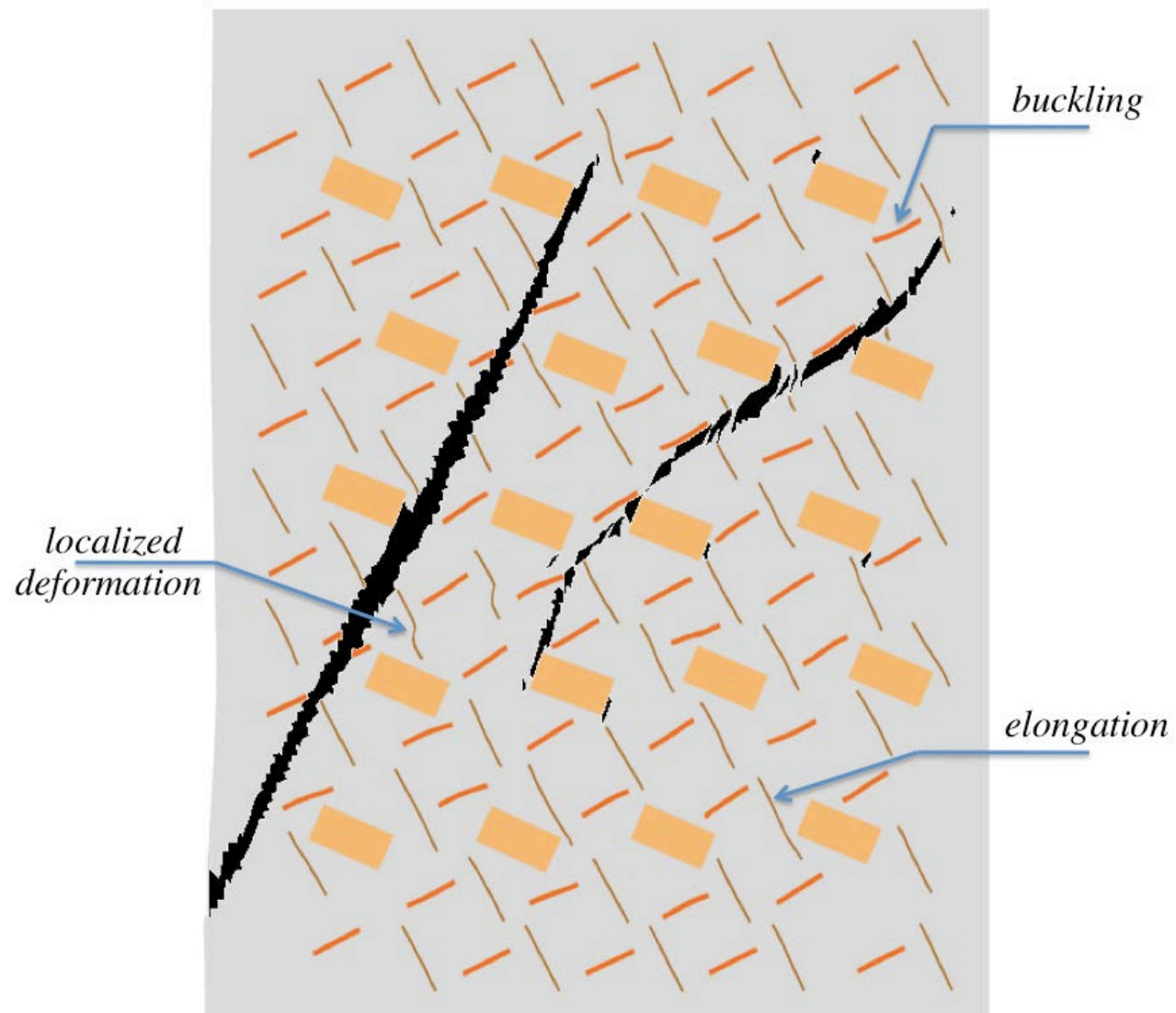
Figure 17: Ruptured microstructure for model 3, showing different deformation modes for the Ω and θ' precipitates, as well as un-deformed Mn-bearing particles
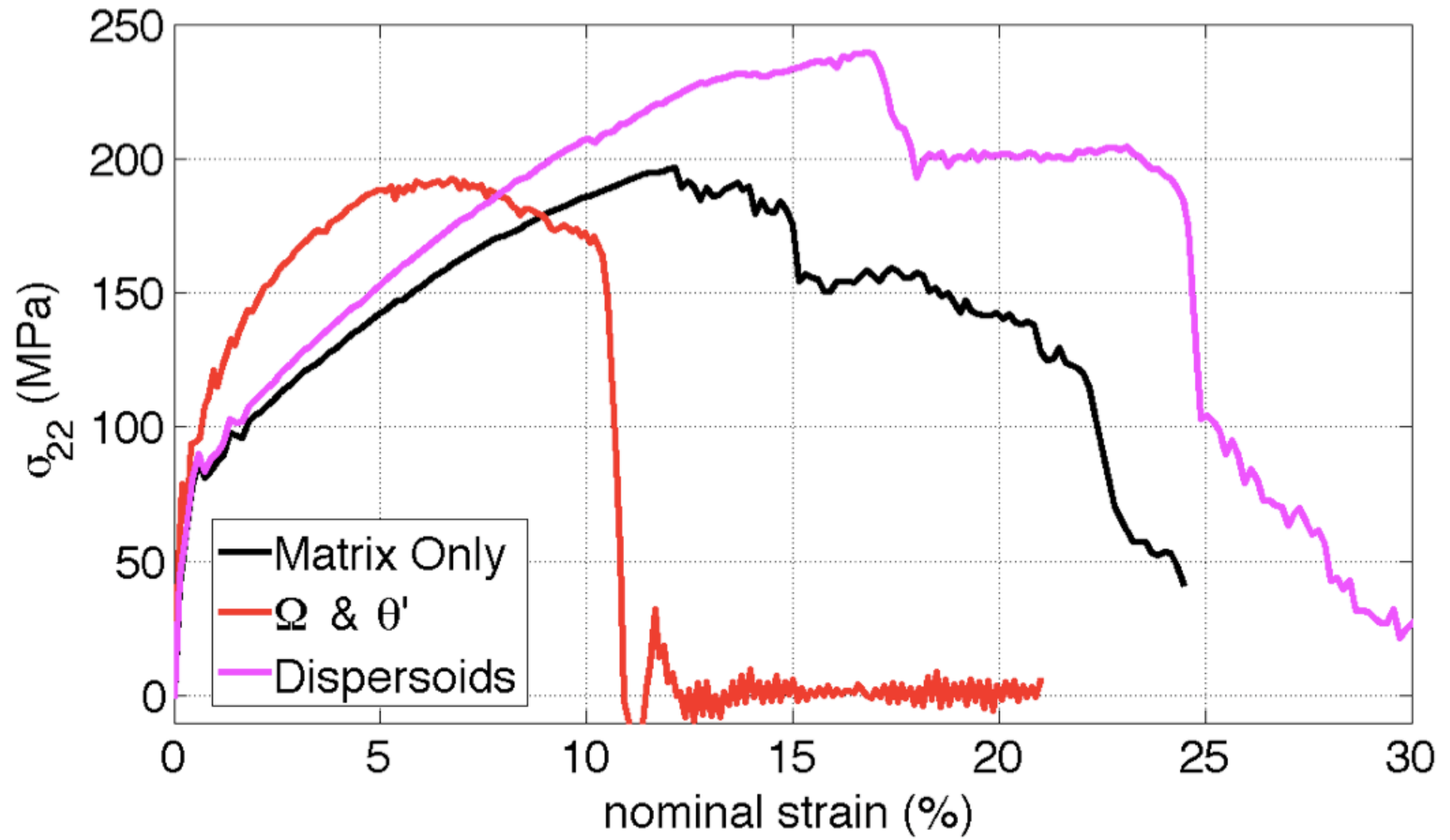
Figure 18: Stress-strain behavior for models with an edge-crack
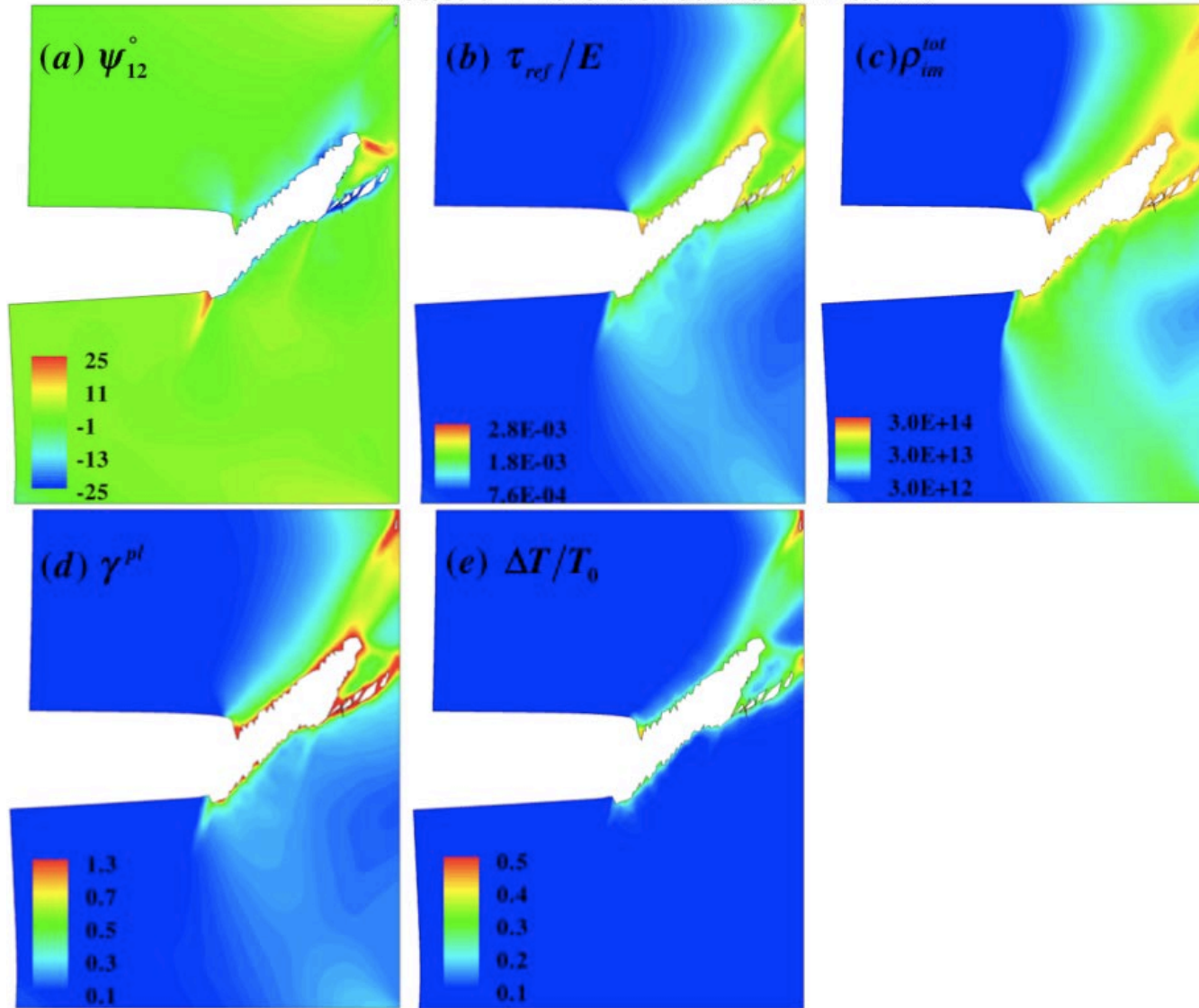
Figure 19: State variables for ruptured pure matrix with an edge crack
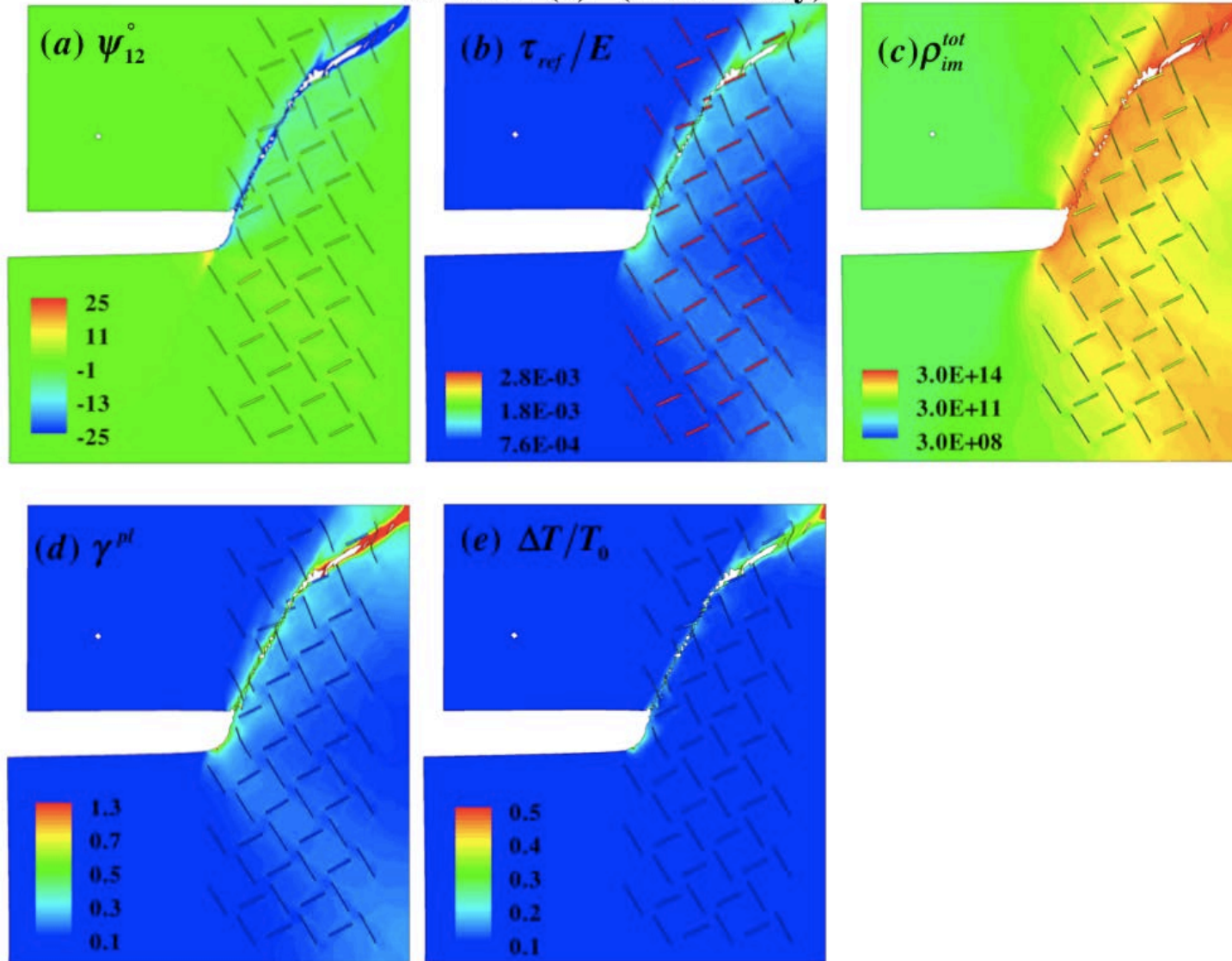
Figure 20: State variables for ruptured microstructure with Ω and θ' precipitates and an edge crack (model 5)
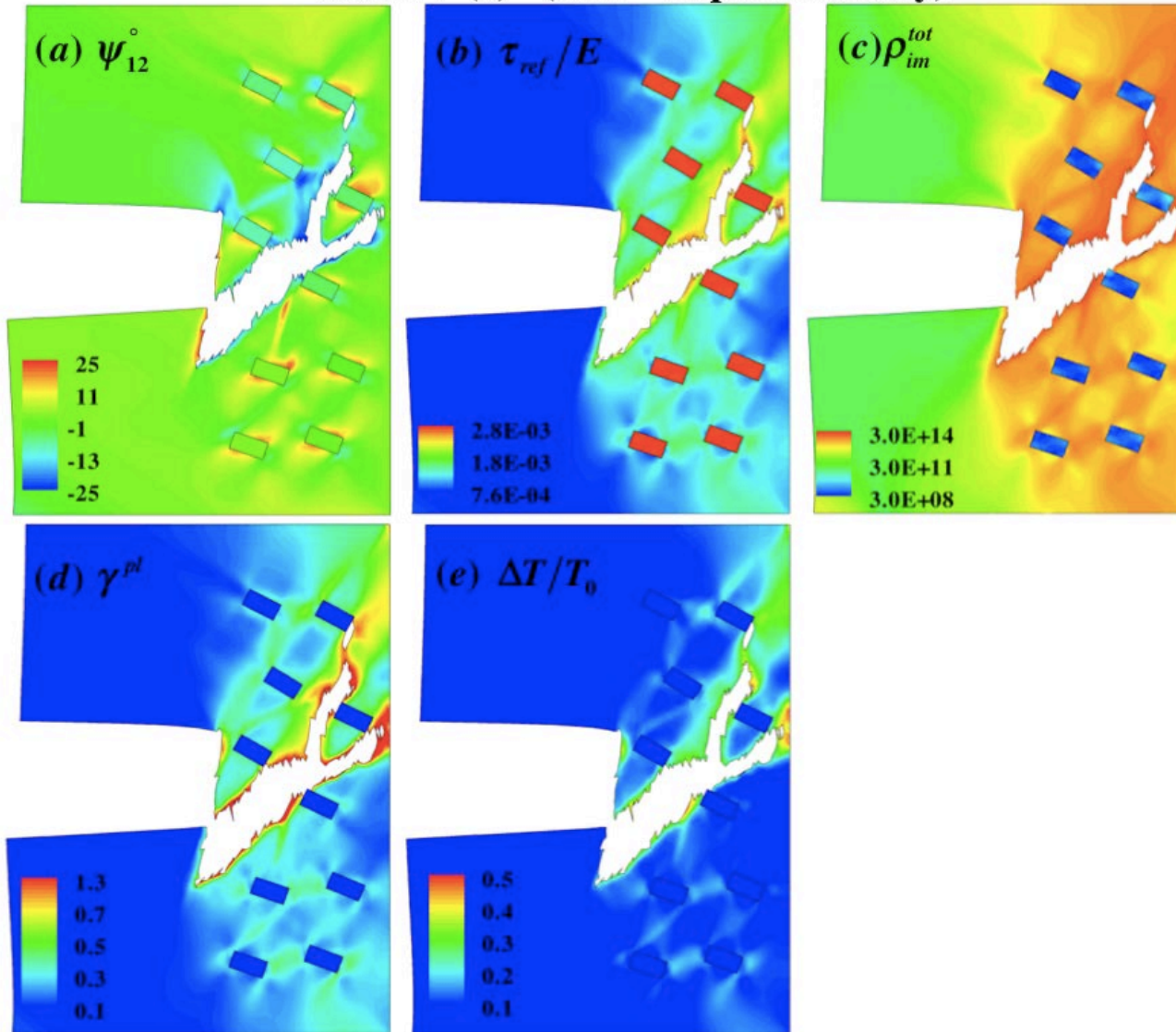
Figure 21: Ruptured microstructure with Mn-bearing particles and an edge-crack (model 6)

Area of Mn-bearing particle = 180x area of a precipitate;
Width of Mn-bearing particle = 60x thickness of a precipitate
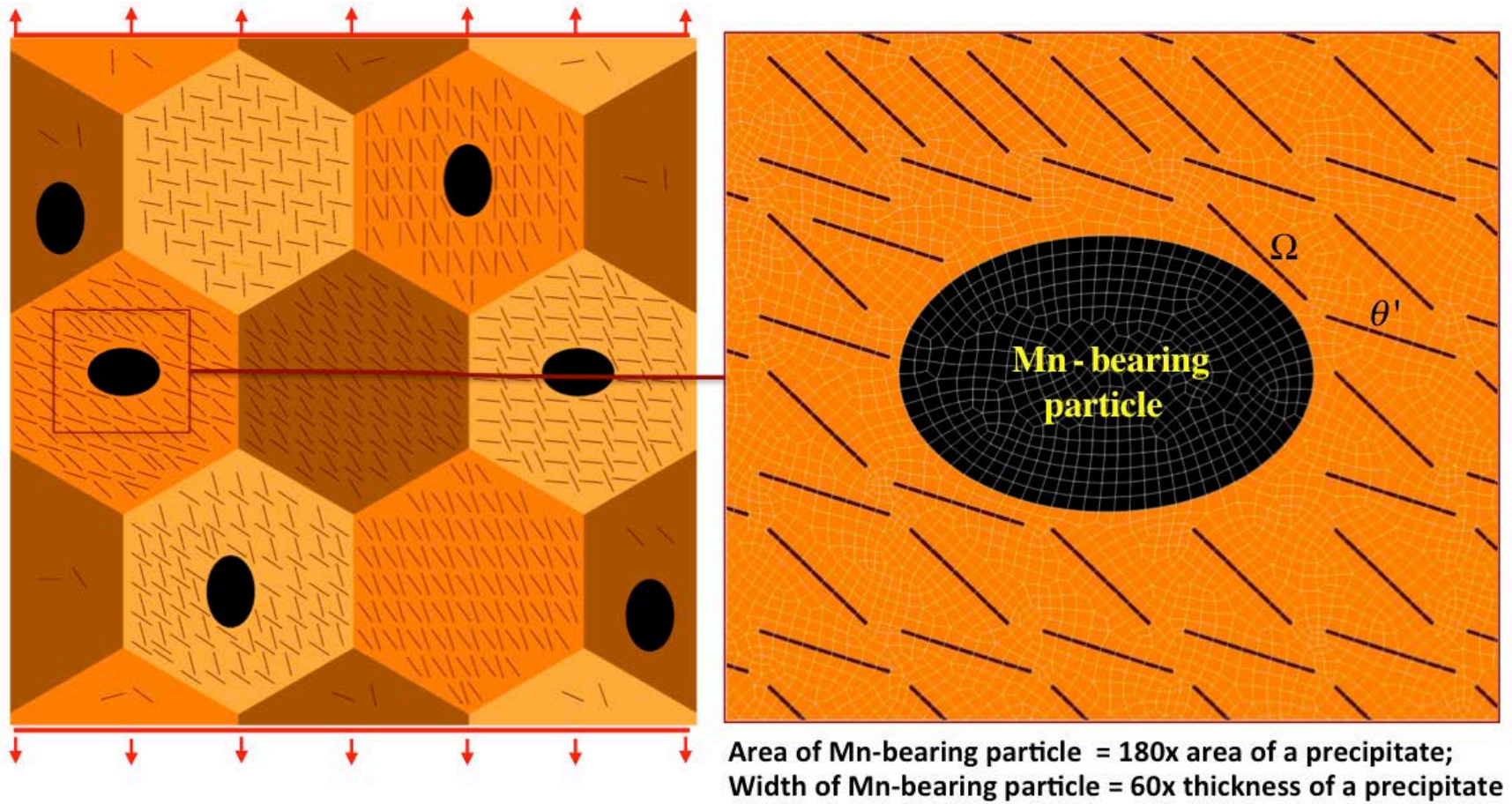
Figure 22: Polycrystalline Aggregate with Ω, θ' and Mn-bearing Particles in the Microstructure.
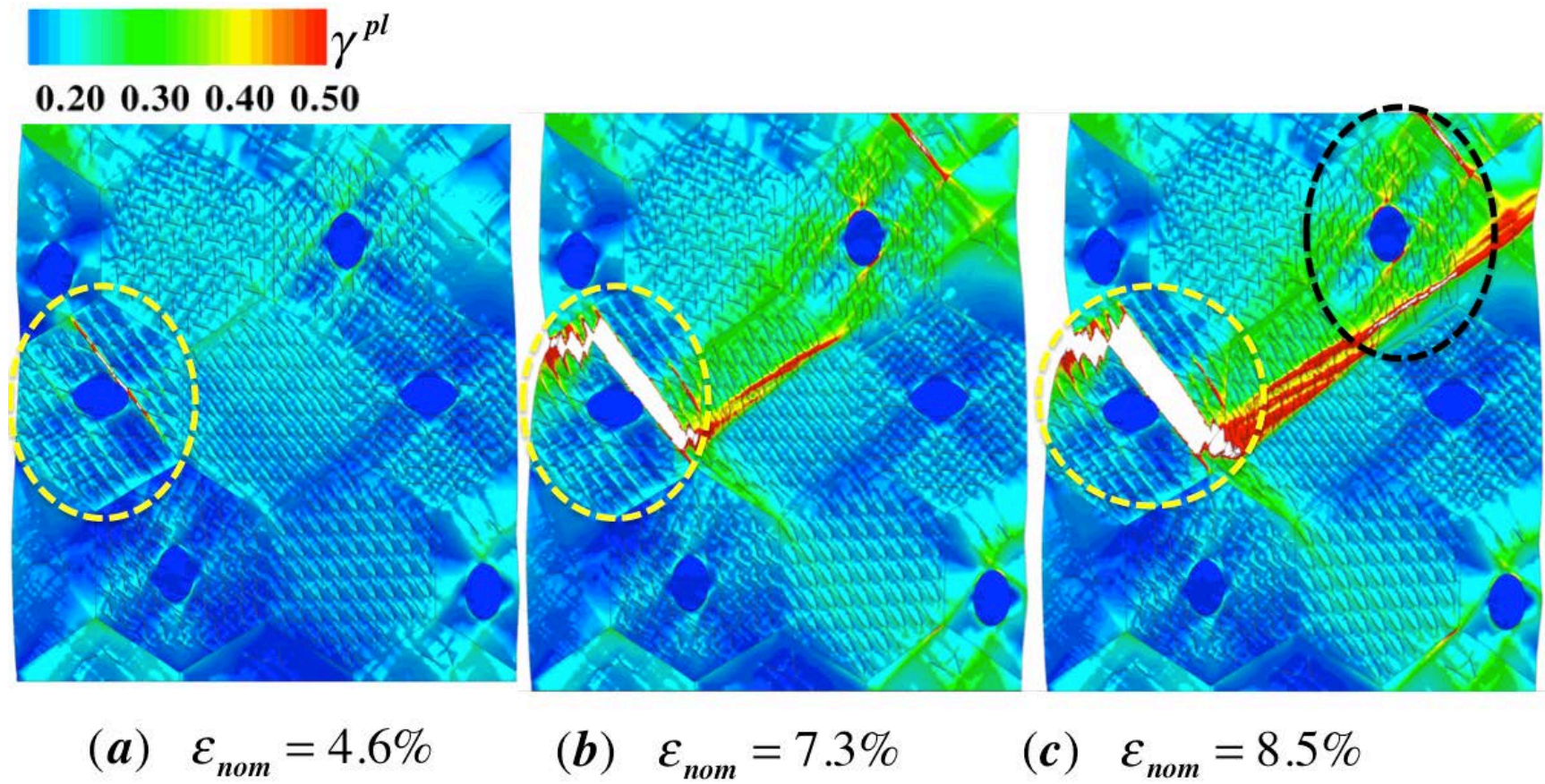
Figure 23: Accumulated Plastic Shear Slip (γ^{pl}) in the grain aggregate.
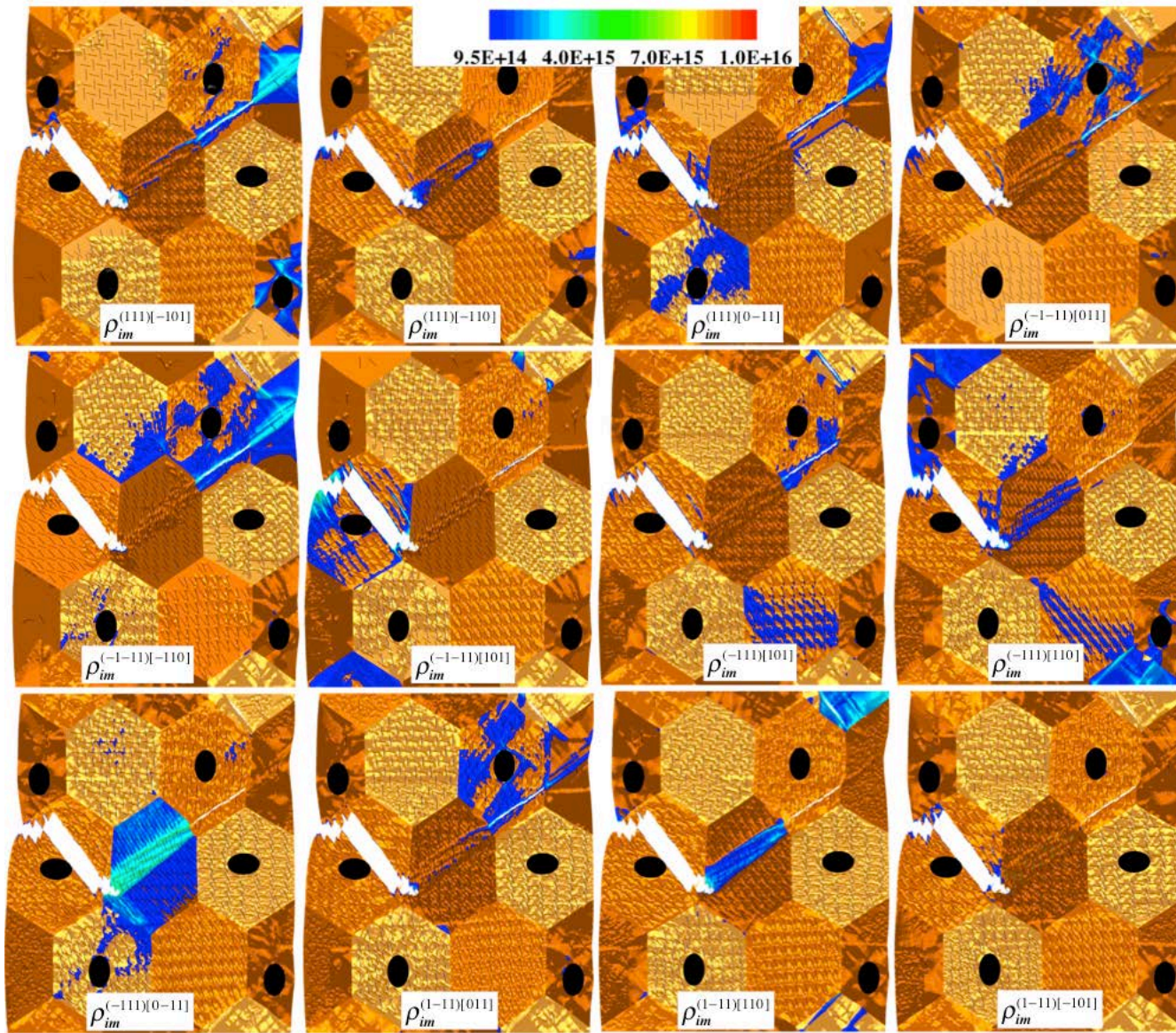
Figure 24: Immobile dislocation density evolution across the 17 grain aggregate
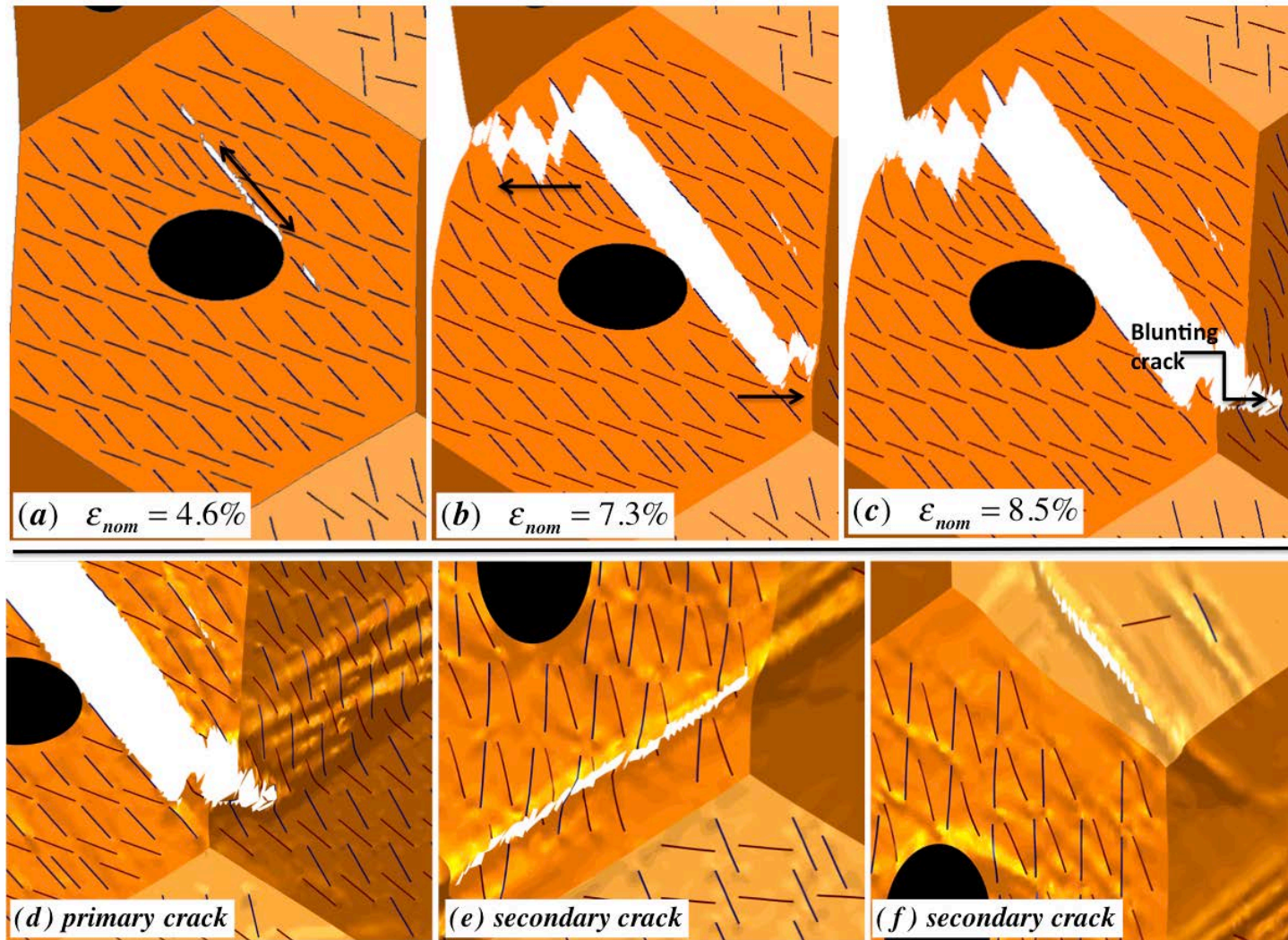
Figure 25: Crack Patterns in grain aggregate. (a-c) Evolving primary crack, (d-f) comparing primary and secondary crack profiles (with shading corresponding to plastic shear slip). The primary crack blunts as it moves to the neighboring grain, whereas secondary cracks are sharp (i.e. roughly one element wide (~50nm), which is the maximum resolution possible with element deletion).

List of Figures

55